Many-Body Theory of Proton-Generated Point Defects for Losses of Electron Energy and Photons in Quantum Wells

Danhong Huang, Andrii Iurov, Fei Gao, Godfrey Gumbs, and D. A. Cardimona

Phys. Rev. Applied **9**, 024002 — Published 6 February 2018

DOI: 10.1103/PhysRevApplied.9.024002

Many-body theory on proton-generated point defects for losses of electron energy and photons in quantum wells

Danhong Huang[1], Andrii Iurov[2], Fei Gao[3], Godfrey Gumbs[4] and D. A. Cardimona[1]

[1] *Air Force Research Laboratory, Space Vehicles Directorate,*
Kirtland Air Force Base, NM 87117, USA

[2] *Center for High Technology Materials, University of New Mexico,*
1313 Goddard SE, Albuquerque, NM, 87106, USA

[3] *Department of Nuclear Engineering and Radiological Sciences,*
University of Michigan, 500 S. State Street, Ann Arbor, MI 48109, USA

[4] *Department of Physics and Astronomy,*
Hunter College of the City University of New York,
695 Park Avenue, New York, NY 10065, USA

(Dated: January 2, 2018)

Abstract

The effects of point defects on the loss of either energies of ballistic electron beams or incident photons are studied by using a many-body theory in a multi-quantum-well system. This includes the defect-induced vertex correction to a bare polarization function of electrons within the ladder approximation as well as the intralayer and interlayer screening of defect-electron interactions are also taken into account in the random-phase approximation. The numerical results of defect effects on both energy-loss and optical-absorption spectra are presented and analyzed for various defect densities, number of quantum wells, and wave vectors. The diffusion-reaction equation is employed for calculating distributions of point defects in a layered structure. For completeness, the production rate for Frenkel-pair defects and their initial concentration are obtained based on atomic-level molecular-dynamics simulations. By combining defect-effect, diffusion-reaction and molecular-dynamics models proposed in this paper with a space-weather forecast model, it will be possible to enable specific designing for electronic and optoelectronic quantum devices that will be operated in space with radiation-hardening protection, and therefore, will effectively extend the lifetime of these satellite onboard electronic and optoelectronic devices. Specifically, this theory can assist a better characterization of quantum-well photodetectors not only for high quantum efficiency and low dark current density but also for radiation tolerance or mitigating the effects of the radiation.

PACS numbers:

I. INTRODUCTION

Point defects (vacancies and interstitials) are produced by displacements of atoms from their thermal-equilibrium lattice sites, [1, 2] where the lattice-atom displacements are mainly caused by a proton-irradiation induced primary knock-on atom (PKA) on a time scale shorter than 100 ps for building up point defects without thermal reactions. These initial displacements are followed immediately by defect mutual recombinations or reactions with sinks (clustering or dissolution of clusters for point-defect stabilizations) [3, 4] on a time scale shorter than 10 ns, then possibly by thermally-activated defect migrations [5] up to a time scale much longer than 10 ns (steady-state distributions). Such atom displacements depend not only on the energy-dependent flux of protons but also on the differential energy transfer cross sections (probabilities) for collision between atoms, interatomic Coulomb interactions and even kinetic-energy loss to core-level electrons of an atom (ionizations). The sample temperature at which the irradiation has been done also significantly affects the diffusion of defects, their stability as clusters and the formation of Frenkel pairs. [6] One of the effective calculation methods for studying the non-thermal spatial-temporal distributions of proton-irradiation-induced point defects is the molecular-dynamics (MD) model [7]. However, the system size increases quadratically with the initial kinetic energy of protons and the time scale can easily run up to several hundred picoseconds. In this case, the defect reaction process driven by thermal migration cannot be included in the MD model due to its much longer time scale. Practically, if the system time evolution goes above 100 ps, either the kinetic lattice Monte-Carlo [8] or the diffusion-reaction equation [9, 10] method should be used instead.

In the presence of defects, dangling bonds attached to these point defects can capture Bloch electrons through multi-phonon emission to form localized charged centers. The randomly-distributed charge centers will further affect electron responses to either an external ballistic electron beam [11] or incident photons [12]. Physically, the defect modifications to the electron response function can be addressed by a vertex correction [12] to a bare electron polarization function in the ladder approximation [13] (LA). In addition, both the intralayer and interlayer screening corrections in a multi-quantum-well system can be included by using the random-phase approximation [13, 14] (RPA). The many-body theory presented here is crucial for understanding the full mechanism for characterizing defects, [15] defect effects, [16] as well as for developing effective mitigation in early design stages of electronic devices. Equipped with this multi-timescale microscopic theory, [17] the experimental characterization of post-irradiated test devices [19] is able to provide useful information on the device architecture's susceptibility to space radiation effects [18]. Furthermore, our physics model should also allow for accurate prediction of device-performance degradation by using the space weather forecast [20, 21] for a particular orbit. With this paper, we expect to bridge the gap between researchers studying radiation-induced damage in materials [1, 2, 22, 23] and others characterizing irradiation-induced performance degradation in devices. [24, 25]

As for applications of the current theory, we would like to emphasize that space-based infrared (IR) imaging is expected to face the most stringent performance requirements on the quantum-well (QW) focal plane array (FPA) [26, 27] due to the high payload cost, complexity, and remoteness the space environment imparts as well as the order of magnitude or more lower incident photon-flux levels that occur in space environments compared to terrestrial ones. Space applications also set up the unique requirement of radiation tolerance (or rad-hardness) on two elements of the hybridized QW-FPA, i.e., the Si-CMOS (complementary metal-oxide-semiconductor) read-out integrated circuit and the photodetector array. FPAs developed for these purposes in a space environment are meticulously characterized for their sensitivity, uniformity, operability and radiation hardness. IR detector arrays operated in the space environment are subjected to a variety of radiation sources while in orbit, e.g., electrons, protons and some heavy ions confined by the earth's magnetic field (Van Allen radiation belts). This indicates that QW photodetectors for space-based surveillance or space-situational awareness must be characterized in advance and should acquire not only high performance (high quantum efficiency and low dark current density) [28, 29] but also radiation tolerance or ability to withstand the effects of the radiation they would expect to encounter in a given orbit. Detector technologies that operate in the harsh radiation environment of space with better radiation tolerance would lead to greater flexibility in orbit selection, technical applications, and system sustainability, and therefore, are of more value to the space-based sensing community.

The rest of the paper is organized as follows. In Sec. II, we present our theoretical model and numerical results to highlight the defect effects on losses of electron energy and photons in multi-quantum-well systems, where defect potentials and vertex corrections, defect effects on partial and total polarization functions, electron-energy loss functions and intrasubband and intersubband absorption spectra have been demonstrated and analyzed. In Sec. III, ultrafast dynamics related to defect production, as well as the follow-up defect diffusion and reaction, will be studied and a steady-state one-dimensional distribution function of point defects will be calculated to provide a direct input for modeling defect effects discussed in Sec. II. Finally, a summary and some remarks are presented in Sec. IV.

II. EFFECTS OF POINT DEFECTS

In Sect. II, we first look into effects of point defects on the electron polarization function in a single wide quantum well. After generalizing the system to multiple quantum wells, we further study the kinetic-energy loss of a parallel (or perpendicular) electron beam. For a comparison, we also calculate the loss of incident photons with a field polarization parallel (or perpendicular) to the quantum-well planes, corresponding to intrasubband [30] (or intersubband [31]) optical transitions of electrons, respectively.

A. Effects on Electron Polarization Function

Since the wave functions of individual point defects are spatially localized, we expect that the interaction between electrons and charged point defects can only affect the screening to the intralayer Coulomb interaction. Therefore, we start with a study of defect effects in a single quantum well. The exchange-interaction-induced vertex correction to a bare polarization function of electrons in a quantum well has been addressed before [12] within the ladder approximation.

For an n-doped quantum well, the total electron polarization function [32] can be written as a sum of partial polarization functions, i.e., $\tilde{\chi}(q_\parallel,\,\omega)=\sum\limits_{n\leq n'}\chi_{n,n'}(q_\parallel,\,\omega)$, where $q_\parallel$ is an electron wavenumber, ω is an angular frequency of an electrical (or optical) perturbation, and $n\leq n'=1,\,2,\,\cdots$ label different energy subbands. Here, each partial polarization function $\chi_{n,n'}(q_\parallel,\,\omega)$ can be calculated through an inverse dielectric function $\mathcal{K}_{n,n';\,m,m'}(q_\parallel,\,\omega)$, according to [11]

$$\chi_{n,n'}(q_\|,\,\omega)=\sum_{m\leq m'}\mathcal{K}_{n,n';\,m,m'}(q_\|,\,\omega)\,\chi^{(0)}_{m,m'}(q_\|,\,\omega)\,\Gamma_{m,m'}(q_\|,\,\omega)\ , \tag{1}$$

where $\Gamma_{m,m'}(q_\|,\,\omega)$ represents a defect-vertex correction, which is determined by Eq. (7) below, and the bare polarization function $\chi^{(0)}_{n,n'}(q_\|,\,\omega)$ takes the form

$$\chi^{(0)}_{m,m'}(q_\|,\,\omega)=\frac{1}{2\pi^2}\int\limits_0^\infty k_\| dk_\|\int\limits_0^{2\pi}d\theta_{\mathbf{k}_\|,\mathbf{q}_\|}$$

$$\times\left\{\frac{f_0[\varepsilon_m(k_\|)]-f_0[\varepsilon_{m'}(|\mathbf{k}_\|+\mathbf{q}_\||)]}{\hbar\omega+i\gamma_0-\varepsilon_{m'}(|\mathbf{k}_\|+\mathbf{q}_\||)+\varepsilon_m(k_\|)}+\frac{f_0[\varepsilon_{m'}(|\mathbf{k}_\|+\mathbf{q}_\||)]-f_0[\varepsilon_m(k_\|)]}{\hbar\omega+i\gamma_0-\varepsilon_m(k_\|)+\varepsilon_{m'}(|\mathbf{k}_\|+\mathbf{q}_\||)}\right\}\ , \tag{2}$$

$\theta_{\mathbf{k}_\|,\mathbf{q}_\|}$ is the angle between wave vectors $\mathbf{k}_\|$ and $\mathbf{q}_\|$, γ_0 is the level broadening, $\varepsilon_n(k_\|)=\varepsilon_n+\hbar^2k_\|^2/2\mu^*$ are subband energies, $\varepsilon_n=\pi^2\hbar^2n^2/2\mu^*L_W^2$, μ^* is the effective mass, L_W is the well width, $f_0(x)=\{1+\exp[(x-u_c)/k_BT]\}^{-1}$ is the Fermi function, u_c and T are the chemical potential and temperature of electrons, respectively.

In addition, the inverse dielectric function $\mathcal{K}_{\ell,\ell';\,m,m'}(q_\|,\,\omega)$ in Eq. (1) satisfies

$$\sum_{m\leq m'}\mathcal{K}_{\ell,\ell';\,m,m'}(q_\|,\,\omega)\,\epsilon_{m,m';\,n,n'}(q_\|,\,\omega)=\delta_{\ell,n}\,\delta_{\ell',n'}\ , \tag{3}$$

where $\epsilon_{m,m';\,n,n'}(q_\|,\,\omega)$ is the dielectric function and can be calculated within the RPA [14] as (right panel of Fig. 1)

$$\epsilon_{m,m';\,n,n'}(q_\|,\,\omega)=\delta_{m,n}\,\delta_{m',n'}-\chi^{(0)}_{n,n'}(q_\|,\,\omega)\,\Gamma_{n,n'}(q_\|,\,\omega)\,\mathcal{V}_{m,m';\,nn'}(q_\|)\ , \tag{4}$$

and the second term corresponds to the defect correction. In Eq. (4), $\mathcal{V}_{m,m';\,n,n'}(q_\|)$ are the intralayer Coulomb matrix elements, given by [33]

$$\mathcal{V}_{m,m';\,n,n'}(q_\|)=\frac{e^2}{2\epsilon_0\epsilon_d(q_\|+q_s)}\int dz\int dz'\ [\mathcal{F}_m(z)]^*\,\mathcal{F}_{m'}(z)\,\mathrm{e}^{-q_\||z-z'|}\ [\mathcal{F}_n(z')]^*\,\mathcal{F}_{n'}(z')\ , \tag{5}$$

where ϵ_d is the host-material dielectric constant, $\mathcal{F}_n(z)=\sqrt{2/L_W}\,\sin[(n\pi/L_W)(z+L_W/2)]$ is the wave function of the nth subband, and

$$q_s=\frac{e^2}{2\pi\epsilon_0\epsilon_d}\sum_n\int\limits_0^\infty k_\| dk_\|\left(-\frac{\partial f_0[\varepsilon_n(k_\|)]}{\partial\varepsilon_n(k_\|)}\right)\ , \tag{6}$$

which plays the role of the inverse of a static screening length. [33] The particle-in-a-box model for electrons in a quantum well is not only a reliable model for a number of existing realistic situations in semiconductor physics but also proves helpful for considering a simple mathematical model to reveal the details of an otherwise complicated theory for effects of defects. Furthermore, this model has been established to work satisfactorily for electrons in wide quantum wells with a high potential barriers and low electron density for which tunneling is insignificant. Therefore, the overlap of electron wave functions in adjacent wells becomes negligible.

For the defect-vertex correction [12] $\Gamma_{n,n'}(q_\parallel,\,\omega)$ introduced in Eqs. (1) and (4), we find the following self-consistent equation within the LA (left panel of Fig. 1)

$$\Gamma_{n,n'}(q_\parallel,\,\omega)=1+\left(\frac{Z^*e^2}{2\epsilon_0\epsilon_d}\right)^2\frac{1}{2\pi^2}\int\limits_0^\infty p_\parallel dp_\parallel\,\chi^{(0)}_{n,n'}(p_\parallel,\,\omega)\,\Gamma_{n,n'}(p_\parallel,\,\omega)$$

$$\times\delta\left[\varepsilon_{n'}\left(\frac{q_\parallel}{2}\right)-\varepsilon_n\left(\frac{p_\parallel}{2}\right)\right]\int\limits_{-\mathcal{L}_0/2}^{\mathcal{L}_0/2}dz_0\,\rho_d(z_0)\,\left|U_{n,n'}(q_\parallel,\,p_\parallel|z_0)\right|^2$$

$$=1+\left(\frac{Z^*e^2}{2\epsilon_0\epsilon_d}\right)^2\frac{2\mu^*}{\pi^2\hbar^2}\,\chi^{(0)}_{n,n'}(q_\parallel^*,\,\omega)\,\Gamma_{n,n'}(q_\parallel^*,\,\omega)\,\left(\int\limits_{-\mathcal{L}_0/2}^{\mathcal{L}_0/2}dz_0\,\rho_d(z_0)\,\left|\overline{U}_{n,n'}(q_\parallel,z_0)\right|^2\right)\,,\qquad(7)$$

where $q_\parallel^*=\sqrt{q_\parallel^2+8\mu^*\varepsilon_{n'n}/\hbar^2}$, $\varepsilon_{n'n}=\varepsilon_{n'}-\varepsilon_n\geq 0$, and the defect interaction with electrons $\left|\overline{U}_{n,n'}(q_\parallel,\,z_0)\right|^2\equiv\left|U_{n,n'}(q_\parallel,\,q_\parallel^*|z_0)\right|^2$ is calculated as

$$\left|\overline{U}_{n,n'}(q_\parallel,\,z_0)\right|^2=\int\limits_0^\pi d\theta\,\left(\frac{\mathrm{e}^{-\Delta^2_{n'n}(q_\parallel,\,\theta)\Lambda_\parallel^2/4}}{\Delta_{n'n}(q_\parallel,\,\theta)+q_s}\right)^2$$

$$\times\left(\int\limits_0^{L_W/2}dz\,\mathcal{F}_n(z)\mathcal{F}_{n'}(z)\,\left[\mathrm{e}^{-\Delta_{n'n}(q_\parallel,\,\theta)|z-z_0|}\pm\mathrm{e}^{-\Delta_{n'n}(q_\parallel,\,\theta)|z+z_0|}\right]\right)^2\,,\qquad(8)$$

the sign $+$ $(-)$ corresponds to the case with $n=n'=1$ or 2 ($n'=2$ and $n=1$), $\mathcal{L}_0$ is the system size, Z^* is the trapped charge number of a point defect, $2\Delta^2_{n'n}(q_\parallel,\,\theta)=q_\parallel^2-q_\parallel\sqrt{q_\parallel^2+8\mu^*\varepsilon_{n'n}/\hbar^2}\,\cos\theta+4\mu^*\varepsilon_{n'n}/\hbar^2$, $\Lambda_\parallel$ is the correlation length for randomly-distributed point defects, and $\rho_d(z_0)$ stands for the one-dimensional distribution function of point defects to be determined later in Sec. III A. Here, $\int_{-\mathcal{L}_0/2}^{\mathcal{L}_0/2}dz_0\,\rho_d(z_0)\left|\overline{U}_{1,2}(q_\parallel,\,z_0)\right|^2=0$ if $\rho_d(z_0)=\rho_d(-z_0)$.

The lowest-order approximate result of Eq. (7) can be obtained simply by replacing $\Gamma_{n,n'}(p_\|,\,\omega)$ with 1 on the right-hand side of this equation. Therefore, the correction to $\Gamma_{n,n'}(q_\|,\,\omega)\approx 1$ becomes proportional to the total number of point defects or integral of $|\overline{U}_{n,n'}|^2$ with respect to z_0. In general, the solution of Eq. (7) includes all the higher orders of $|\overline{U}_{n,n'}|^2$ by going beyond the second-order Born approximation [34].

The results calculated from Eq. (8) for $|\overline{U}_{n,n'}(q_\|,\,z_0)|^2$ are shown in Fig. 2, where the features in $|\overline{U}_{n,n}|^2$ with $n=1,\,2$ for intrasubband interactions in Figs. 2(a) and 2(c) result from the symmetry and anti-symmetry properties of the first two electron wave functions in a quantum well. On the other hand, $|\overline{U}_{1,2}|^2$ in Fig. 2(b) for intersubband interactions displays the overlap of these two electron wave functions with opposite symmetries, leading to two peaks and one node around $z_0=0$. From Figs. 2(a) and 2(c) we further find that both the peak strength and peak width decrease with increasing $q_\|$, and the reduction of peak strength with $q_\|$ can be seen more clearly from Fig. 2(d). In addition, a finite value of $\Delta_{21}(q_\|,\,\theta)$ at $q_\|=0$ leads to a negligible $|\overline{U}_{1,2}|^2$, and furthermore, the widths of the dual peaks in Fig. 2(b) spread out significantly with $q_\|$.

Based on the calculated $|\overline{U}_{n,n'}(q_\|,\,z_0)|^2$ in Fig. 2, Eq. (7) can be applied to compute the dynamical defect-vertex correction $\Gamma_{n,n'}(q_\|,\,\omega)$ with respect to unity in the ladder approximation. In order to simulate the physical distribution of defects shown in Fig. 9, we assume a regional form, i.e., $\rho_d(z_0)/\kappa=\rho_1\Theta(-z_0-L_W/2)+\rho_2\Theta(z_0-L_W/2)+[\rho_0+z_0(\Delta\rho/L_W)]\Theta(L_W/2-|z_0|)$, where $\Theta(x)$ is a unit-step function and κ is a scaling number. Similar dependences on both ω and $q_\|$ are seen in Figs. 3(a) and 3(b), respectively, where a very strong intrasubband-scattering resonance associated with a sign switching in $\text{Re}[\Gamma_{n,n}(q_\|,\,\omega)]-1$ ($q_\|=q_\|^*$ for $n=n'=1,\,2$) occurs only within the small-value $q_\|$-ω region due to the presence of the $\chi^{(0)}_{n,n}(q_\|,\omega)$ interaction term in Eq. (7). In this case, the intrasubband-scattering resonance is determined by the peak of

$$\Gamma_{n,n}(q_\|,\,\omega)=\left[1-\left(\frac{Z^*e^2}{2\epsilon_0\epsilon_d}\right)^2\frac{2\mu^*}{\pi^2\hbar^2}\,\chi^{(0)}_{n,n}(q_\|,\,\omega)\left(\int\limits_{-\mathcal{L}_0/2}^{\mathcal{L}_0/2}dz_0\,\rho_d(z_0)\,\left|\overline{U}_{n,n}(q_\|,z_0)\right|^2\right)\right]^{-1}\,. \quad (9)$$

The strength of this intrasubband-scattering resonance decreases rapidly with increasing $q_\|$ due to reduced $|\overline{U}_{n,n}(q_\|,z_0)|^2$ from the suppressed long-range intrasubband scattering as displayed in Fig. 2(d). For intersubband excitation with $n=1$ and $n'=2$, on the other hand, the two $\Gamma_{1,2}$ terms with $q_\parallel$ and $q_\parallel^* = \sqrt{q_\parallel^2 + 8\mu^*\varepsilon_{21}/\hbar^2}$ are coupled to each other as can be verified by Eq. (7). As a result, the broad intersubband-scattering resonance shows up in Figs. 3(c) and 3(d) along with a sign switching in $\mathrm{Re}[\Gamma_{1,2}(q_\parallel,\,\omega)] - 1$ and a peak in $\mathrm{Im}[\Gamma_{1,2}(q_\parallel,\,\omega)]$. Furthermore, it is very important to notice that the broad intersubband-scattering resonance in Figs. 3(c) and 3(d), due to elastic coupling between $q_\parallel$ and $q_\parallel^*$ electron states in two subbands, will be different from the sharp intersubabnd-plasmon resonance determined by $\chi_{1,2}^{(0)}(q_\parallel,\,\omega)$ in Eq. (2).

The calculated $\Gamma_{n,n'}(q_\parallel,\,\omega)$ in Fig. 3 has been substituted into Eq. (4) to find the intralayer dielectric function modified by defects in the RPA. Graphically, the dispersion relations of intrasubband-plasmon modes appear as peaks in the density plot for absolute value of the real part of $1/\mathcal{D}et[\overleftrightarrow{\boldsymbol{\epsilon}}(q_\parallel,\omega)]$ within the $(\omega, q_\parallel)$-plane, where the dielectric-function matrix $\overleftrightarrow{\boldsymbol{\epsilon}}(q_\parallel,\omega)$ has been defined in Eq. (4). In the absence of defects, from Figs. 4(a) and 4(c) we find two intrasubband-plasmon modes and two particle-hole continua (i.e., $\mathrm{Im}\{\chi_{n,n}^{(0)}(q_\parallel,\omega)\}$), correspondingly, for two occupied subbands in a quantum well. By further introducing defects to the quantum well in Fig. 4(b), the dispersion of the lower plasmon mode has been modified noticeably for small q_x values due to energy shifts from the contribution of $\mathrm{Re}\{\Gamma_{n,n}(q_\parallel,\omega)\}$ as shown in Fig. 3. Such a modification to the plasmon dispersion relation can have a nonlinear κ dependence for large κ values (or higher defect densities). The defect effect on the intersubband-plasmon mode is very weak and not shown in Fig. 4.

By using Eq. (3) with this modified dielectric function, the resulting inverse dielectric function has further been input into Eq. (1) to compute related changes in the screened partial polarization functions $\delta\chi_{n,n'}(q_\parallel,\,\omega)$ of a single quantum well. For intrasubband excitations in Figs. 5(a) and 5(c), the defect-induced change $\delta\mathrm{Im}[\chi_{1,1}(q_\parallel,\,\omega)]$ displays a peak shift (sign switching) to a lower and lower value of ω with increasing κ. However, $\delta\mathrm{Im}[\chi_{1,1}(q_\parallel,\,\omega)]$ reduces significantly for a larger $q_\parallel$ value due to weakened scattering interaction as shown in Fig. 2(d). It is also interesting to notice that the depolarization shift of a plasmon peak ($\mathrm{Im}[\chi_{1,1}(q_\parallel,\,\omega)]$ vs. $\mathrm{Im}[\chi_{1,1}^{(0)}(q_\parallel,\,\omega)]$) in the two insets of ($i1$) and ($i3$) (with $\Gamma_{n,n'}(q_\parallel,\,\omega) \equiv 1$) also increases with $q_\parallel$, but it will not show up in $\delta\mathrm{Im}[\chi_{1,1}(q_\parallel,\,\omega)]$ for defect effects. This pure plasmon depolarization shift to a higher ω value is rooted in a many-body screening effect and is slightly reduced by defect scatterings. Similar features in $\delta\mathrm{Im}[\chi_{1,2}(q_\parallel,\,\omega)]$ can also be found from Fig. 5(d) for intersubband losses, but their magnitudes become much smaller due to very weak intersubband scattering processes. In addition to the shift of this broad intrasubband-plasmon peak by defects, we also expect defect effects on a sharper intersubband-plasmon-loss peak (around $\hbar\omega \sim \varepsilon_{21}$) for a smaller $q_\parallel$ value, as presented in the inset of Fig. 5(b), where nearly no shift of the intensive intersubband-plasmon peak is found.

B. Effects on Energy Loss of Electron Beams

In Sec II A, we discussed effects of defects on the intralayer partial polarization function $\chi_{n,n'}(q_\parallel,\,\omega)$. Here, we extend our study to the kinetic-energy loss of a ballistic electron beam by further taking into account the defect effects on the interlayer total polarization function. A full review on the excitation of collective modes, such as plasmons, in bulk materials, planar surfaces, and nanoparticles was reported, [35] and the light emission induced by the electrons was proven to be an excellent probe of plasmons, combining subnanometer resolution in the position of the electron beam with nanometer resolution in the emitted wavelength.

Let us assume that a semi-infinite semiconductor occupies the $z > 0$ half-space and consider a classical (heavy and slow) point charge Q_0 moving along a prescribed path $\mathbf{R}(t)$ in the air space ($z < 0$) outside the semiconductor region. In such a case, we find that the external potential Φ_{ext} associated with this moving charged particle in the quasi-static limit satisfies the instantaneous Poisson's equation, [36, 37] i.e.

$$\nabla^2_{\mathbf{r}}\Phi_{ext}(\mathbf{r},t|\mathbf{R}) = -\frac{Q_0}{\epsilon_0}\,\delta\left[\mathbf{r}-\mathbf{R}(t)\right]\ , \tag{10}$$

where $\mathbf{R}(t) = \{\mathbf{R}_\parallel(t),\,Z(t)\}$ is the trajectory of the charged particle, and $\mathbf{r} = \{\mathbf{r}_\parallel,\,z\}$ is a position vector. The solution of Eq. (10) inside the region of $Z(t) < z < 0$ is found to be

$$\Phi^<_{ext}(\mathbf{r},t|\mathbf{R}) = \int \frac{d^2\mathbf{q}_\parallel}{(2\pi)^2}\int\limits_{-\infty}^{\infty}\frac{d\omega}{2\pi}\,\phi_{ext}(\mathbf{q}_\parallel,\omega|\mathbf{R})\,e^{i\mathbf{q}_\parallel\cdot\mathbf{r}_\parallel-i\omega t}\,e^{-q_\parallel z}\ , \tag{11}$$

where the Fourier-transformed external potential is calculated as

$$\phi_{ext}(\mathbf{q}_\parallel,\omega|\mathbf{R}) = -\frac{Q_0}{2\epsilon_0 q_\parallel}\,\mathcal{F}_0(\mathbf{q}_\parallel,\omega|\mathbf{R})\ , \tag{12}$$

and its structure factor is

$$\mathcal{F}_0(\mathbf{q}_\parallel,\omega|\mathbf{R}) = \int\limits_{-\infty}^{\infty} dt'\, e^{q_\parallel Z(t')}\, e^{i\omega t' - i\mathbf{q}_\parallel\cdot\mathbf{R}_\parallel(t')}\ . \tag{13}$$

From a physics perspective, the existence of Φ_{ext} inside the semiconductor will induce a potential Φ_{ind} outside the semiconductor (i.e., $z < 0$) due to the charge-density fluctuation, yielding

$$\Phi_{ind}^{<}(\mathbf{r},t|\mathbf{R}) = -\int \frac{d^2\mathbf{q}_\parallel}{(2\pi)^2}\int\limits_{-\infty}^{\infty}\frac{d\omega}{2\pi}\,\phi_{ext}(\mathbf{q}_\parallel,\omega|\mathbf{R})\, e^{i\mathbf{q}_\parallel\cdot\mathbf{r}_\parallel - i\omega t}\,\mathcal{S}(q_\parallel,\,\omega)\, e^{q_\parallel z}\ , \tag{14}$$

where $\mathcal{S}(q_\parallel,\,\omega)$ is the so-called surface-response function [11] determined later by matching the boundary condition. Within the semiconductor region ($0 \leq z \leq \mathcal{L}_0$), we write down similar expressions for the external $\Phi_{ext}^{>}$ and induced $\Phi_{ind}^{>}$ potentials, given by

$$\Phi_{ext}^{>}(\mathbf{r},t|\mathbf{R}) = \int \frac{d^2\mathbf{q}_\parallel}{(2\pi)^2}\int\limits_{-\infty}^{\infty}\frac{d\omega}{2\pi}\,\phi_{ext}(\mathbf{q}_\parallel,\omega|\mathbf{R})\, e^{i\mathbf{q}_\parallel\cdot\mathbf{r}_\parallel - i\omega t}\,\Phi_0^{>}(z|q_\parallel)\ , \tag{15}$$

$$\Phi_{ind}^{>}(\mathbf{r},t|\mathbf{R}) = -\int \frac{d^2\mathbf{q}_\parallel}{(2\pi)^2}\int\limits_{-\infty}^{\infty}\frac{d\omega}{2\pi}\,\phi_{ext}(\mathbf{q}_\parallel,\omega|\mathbf{R})\, e^{i\mathbf{q}_\parallel\cdot\mathbf{r}_\parallel - i\omega t}\,\phi_{ind}^{>}(z|q_\parallel,\omega)\ , \tag{16}$$

where $\Phi_0^{>}(z|q_\parallel)$ is the bare external potential in the electrostatic limit ($q_\parallel c \gg \omega$) for a slab of semiconductor material of thickness $\mathcal{L}_0$, $\Phi_0^{>}(0|q_\parallel) = 1 - g_{slab}(q_\parallel)$, and $g_{slab}(q_\parallel)$ is the surface-response function for a dielectric slab without doping electrons. [11] Since the total potential $\Phi_0^{>}(z|q_\parallel) + \phi_{ind}^{>}(z|q_\parallel,\omega)$ inside the semiconductor ($z > 0$) equals the screened external potential, we get $\phi_{ind}^{>}$ in Eq. (16) from [38]

$$\phi_{ind}^{>}(z|q_\parallel,\omega) = \int dz'\left[\epsilon^{-1}(z,z'|q_\parallel,\omega) - \delta(z-z')\right]\Phi_0^{>}(z'|q_\parallel)\ . \tag{17}$$

In Eq. (17), the inverse dielectric function can be found from

$$\epsilon^{-1}(z,z'|q_\parallel,\omega) = \delta(z-z') + \int dz''\, V_c(z,z''|q_\parallel)\,\chi(z'',z'|q_\parallel,\omega)\ , \tag{18}$$

where the interlayer Coulomb coupling $V_c(z,z'|q_\parallel)$, including the image potentials, is calculated as [11]

$$V_c(z,z'|q_\|)=\frac{\beta_0(q_\|)\,e^2}{2\epsilon_0\epsilon_d(q_\|+q_s)}\left[e^{-q_\||z-z'|}+\alpha_0^2\,e^{-2q_\|\mathcal{L}_0}\,e^{q_\||z-z'|}+\alpha_0\,e^{-q_\||z+z'|}+\alpha_0\,e^{-2q_\|\mathcal{L}_0}\,e^{q_\||z+z'|}\right]\ , \tag{19}$$

and $\alpha_0=(\epsilon_d-1)/(\epsilon_d+1)$, $\beta_0(q_\|)=1/[1-\alpha_0^2\exp(-2q_\|\mathcal{L}_0)]$.

For a multi-quantum-well system, the density-density-response function in Eq. (18) takes the form [36]

$$\chi(z,z'|q_\|,\omega)=\sum_{j,j'=0}^{N}\delta(z-ja)\,\tilde{\chi}_e(j,j'|q_\|,\omega)\,\delta(z'-j'a)\ , \tag{20}$$

where a is the well separation, $\mathcal{L}_0=Na$, and the screened polarization function $\tilde{\chi}_e(j,j'|q_\|,\omega)$ within the RPA can be obtained from the following self-consistent equations [36]

$$\tilde{\chi}_e(j,j'|q_\|,\omega)=\tilde{\chi}_j(q_\|,\,\omega)\,\delta_{j,j'}+\tilde{\chi}_j(q_\|,\,\omega)\sum_{j''(\neq j)=0}^{N}V_c(ja,j''a|q_\|)\,\tilde{\chi}_e(j'',j'|q_\|,\omega)\ . \tag{21}$$

Here, the summation over j'' excludes the intralayer term with $j''=j$, the integers $j=0,\,1,\,\cdots,\,N$ labels different wells, and $\tilde{\chi}_j(q_\|,\,\omega)=\sum\limits_{n\leq n'}\chi_{n,n'}(j,j|q_\|,\omega)$ is the total polarization function for the jth quantum well as discussed in Sec. II A.

By combining Eqs. (17), (18) and (20), $\phi^>_{ind}(z|q_\|,\omega)$ in Eq. (16) can be simply rewritten as

$$\phi^>_{ind}(z|q_\|,\omega)=\sum_{j,j'=0}^{N}V_c(z,ja|q_\|)\,\tilde{\chi}_e(j,j'|q_\|,\omega)\,\Phi_0^>(j'a|q_\|)\ . \tag{22}$$

By matching the boundary condition for the total potential, i.e., $1-\mathcal{S}(q_\|,\,\omega)=[1-g_{slab}(q_\|)]+\phi^>_{ind}(0|q_\|,\omega)$ at the surface $z=0$, we are able to find the surface response function introduced in Eq. (14) from

$$\mathcal{S}(q_\|,\,\omega)=g_{slab}(q_\|)-\sum_{j,j'=0}^{N}V_c(0,ja|q_\|)\,\tilde{\chi}_e(j,j'|q_\|,\omega)\,\Phi_0^>(j'a|q_\|)\ , \tag{23}$$

where [36]

$$g_{slab}(q_\|)=2\alpha_0\,\beta_0(q_\|)\,e^{-q_\|Na}\,\sinh(q_\|Na)\ , \tag{24}$$

and the external electrostatic potential in Eqs. (17) and (23) inside a slab of semiconductor ($0 \leq z \leq Na$) is found to be [36]

$$\Phi_0^>(z|q_\parallel) = \left[\frac{1-g_{slab}(q_\parallel)}{2} + \frac{1+g_{slab}(q_\parallel)}{2\epsilon_d}\right] e^{-q_\parallel z} + \left[\frac{1-g_{slab}(q_\parallel)}{2} - \frac{1+g_{slab}(q_\parallel)}{2\epsilon_d}\right] e^{q_\parallel z} \ . \quad (25)$$

The absorbed kinetic energy $\Delta E_{abs}\{\mathbf{R}\}$ of an electron beam can be calculated by integrating the Poynting vector over the surface and over time in the air region, which leads to [38]

$$\Delta E_{abs}\{\mathbf{R}\} = \epsilon_0 \int d^2\mathbf{r}_\parallel \int\limits_{-\infty}^{\infty} dt\, \mathrm{Re}\left\{[\Phi_{tot}^<(\mathbf{r},t|\mathbf{R})]^* \,\frac{\partial^2 \Phi_{tot}^<(\mathbf{r},t|\mathbf{R})}{\partial t\, \partial z}\right\}\Bigg|_{z=0} \ , \quad (26)$$

where $\Phi_{tot}^<(\mathbf{r},t|\mathbf{R})$ is the total potential outside the semiconductor region ($z<0$), calculated by combining Eqs. (11) and (14) and given by

$$\Phi_{tot}^<(\mathbf{r},t|\mathbf{R}) = \int \frac{d^2\mathbf{q}_\parallel}{(2\pi)^2} \int\limits_{-\infty}^{\infty} \frac{d\omega}{2\pi} \left[e^{-q_\parallel z} - \mathcal{S}(q_\parallel,\,\omega)\, e^{q_\parallel z}\right] e^{i\mathbf{q}_\parallel\cdot\mathbf{r}_\parallel - i\omega t}\, \phi_{ext}(\mathbf{q}_\parallel,\omega|\mathbf{R}) \ . \quad (27)$$

Substituting this result into Eq. (26), we find

$$\Delta E_{abs}\{\mathbf{R}\} = \frac{Q_0^2}{2\epsilon_0} \int \frac{d^2\mathbf{q}_\parallel}{(2\pi)^2} \int\limits_{-\infty}^{\infty} \frac{d\omega}{2\pi} \left(\frac{\left|\mathcal{F}_0(\mathbf{q}_\parallel,\omega|\mathbf{R})\right|^2 \omega}{q_\parallel}\right) \mathrm{Im}\left\{\mathcal{S}(q_\parallel,\,\omega)\right\} \ , \quad (28)$$

where $\mathrm{Im}\left\{\mathcal{S}(q_\parallel,\,\omega)\right\}$ is the so-called loss function. [11]

Specifically, for a charged particle moving parallel to the surface, we have $\mathbf{R}(t) = \{\mathbf{V}_\parallel t,\, Z_0\}$ and obtain

$$\left|\mathcal{F}_0(\mathbf{q}_\parallel,\omega|\mathbf{R})\right|^2 = \lim_{\Delta T\to\infty} \left|\int\limits_{-\Delta T/2}^{\Delta T/2} dt'\, e^{-q_\parallel Z_0}\, e^{i(\omega - \mathbf{q}_\parallel\cdot\mathbf{V}_\parallel)t'}\right|^2 = 2\pi\Delta T\, e^{-2q_\parallel|Z_0|}\,\delta(\omega - \mathbf{q}_\parallel\cdot\mathbf{V}_\parallel) \ , \quad (29)$$

which leads to the following power absorption for the parallel electron beam

$$\frac{\Delta E_{abs}(V_\parallel)}{\Delta T} = \frac{Q_0^2}{2\epsilon_0} \int \frac{d^2\mathbf{q}_\parallel}{(2\pi)^2}\, e^{-2q_\parallel|Z_0|} \left(\frac{\mathbf{q}_\parallel\cdot\mathbf{V}_\parallel}{q_\parallel}\right) \mathrm{Im}\left[\mathcal{S}(q_\parallel,\,\mathbf{q}_\parallel\cdot\mathbf{V}_\parallel)\right] \ . \quad (30)$$

More interesting, if a charged particle moves away from the surface perpendicularly, we can write $\mathbf{R}(t)=\{0,\,Z_0-V_\perp t\}$ with an impact parameter $|Z_0|$ ($Z_0<0$) and $0\leq t\leq T_0$ for the damped particle, and obtain

$$\left|\mathcal{F}_0(\mathbf{q}_\|,\omega|\mathbf{R})\right|^2=\lim_{T_0\to\infty}\left|\int\limits_0^{T_0}dt'\,e^{-q_\|(|Z_0|+V_\perp t')}\,e^{i\omega t'}\right|^2$$

$$=\lim_{T_0\to\infty}\left|\frac{e^{-q_\||Z_0|}}{q_\|V_\perp-i\omega}\,\left[1-e^{(q_\|V_\perp-i\omega)T_0}\right]\right|^2=\frac{e^{-2q_\||Z_0|}}{\omega^2+q_\|^2V_\perp^2}\ , \qquad (31)$$

which yields the energy absorption for the perpendicular electron beam

$$\Delta E_{abs}(V_\perp)=\frac{Q_0^2}{2\epsilon_0}\int\frac{d^2\mathbf{q}_\|}{(2\pi)^2}\int\frac{d\omega}{2\pi}\,\left(\frac{\omega}{q_\|}\right)\,\frac{e^{-2q_\||Z_0|}}{\omega^2+q_\|^2V_\perp^2}\,\mathrm{Im}\left\{\mathcal{S}(q_\|,\,\omega)\right\}\ . \qquad (32)$$

In this case, the integral over ω with respect to the loss function $\mathrm{Im}\{\mathcal{S}(q_\|,\,\omega)\}$ includes the damping contributions from both the particle-hole and collective excitation modes of electrons. [39]

Multiple plasmon excitations in graphene materials by a single electron was predicted to give rise to a unique platform for exploring the bosonic quantum nature of these collective modes. [40] Such a technique not only opens a viable path toward multiple excitation of a single plasmon mode by a single electron, but also reveals electron probes as ideal tools for producing, detecting, and manipulating plasmons in graphene nanostructures.

For a single quantum well, the surface response function $\mathcal{S}(q_\|,\,\omega)=\sum\limits_{n\leq n'}\mathcal{S}_{n,n'}(q_\|,\omega)$ can be obtained by setting $j=j'=0$ in Eq. (23), and the total loss function is just $\mathrm{Im}[\mathcal{S}(q_\|,\,\omega)]=\sum\limits_{n\leq n'}\mathrm{Im}[\mathcal{S}_{n,n'}(q_\|,\omega)]$. Here, the defect induced change $\delta\mathrm{Im}[\mathcal{S}_{n,n'}(q_\|,\omega)]$ directly relates to the imaginary part of the screened partial polarization function $\delta\mathrm{Im}[\chi_{n,n'}(q_\|,\omega)]$ presented in Fig. 5. For $q_\|/k_F=1.0$, we find from Figs. 6(a) and 6(c) that $\delta\mathrm{Im}[\mathcal{S}(q_\|,\,\omega)]$ is dominated by $\delta\mathrm{Im}[\mathcal{S}_{1,1}(q_\|,\,\omega)]$ for a stronger intrasubband scattering process, which increases with the defect-density scaling number κ. The sign switching reflects the shift of a loss peak [see insets of Figs. 6(a) and 6(c)] to a lower value of ω. As $q_\|/k_F$ is increased to 2.5 in Figs. 6(b) and 6(d), the resonant peak of $\mathrm{Im}[\mathcal{S}(q_\|,\,\omega)]$ moves to a higher ω value [comparing (i1)-(i2) and (i3)-(i4)]. However, the similar defect-related features as in Figs. 6(a) and 6(c) are greatly weakened due to a dramatic reduction of scattering interactions as shown in Fig. 2(d).

For a multi-quantum well system, the interlayer Coulomb coupling $V_c(ja, j'a|q_\|)$ in Eq. (21) will modify the intralayer total polarization function $\tilde{\chi}_j(q_\|,\,\omega)$, as well as the surface response function in Eq. (23). From the comparison of single- and multi-quantum well systems in Fig. 7, we find the intersubband-plasmon loss $\mathrm{Im}[\mathcal{S}_{1,2}(q_\|,\,\omega)]$ is strongly coupled to the intrasubband-plasmon loss $\mathrm{Im}[\mathcal{S}_{1,1}(q_\|,\,\omega)]$ by interlayer Coulomb coupling, as shown in the inset $(i4)$. Here, the weaker $\mathrm{Im}[\mathcal{S}_{1,1}(q_\|,\,\omega)]$ peak in the inset $(i2)$ is greatly enhanced by its sitting on the shoulder of a much stronger $\mathrm{Im}[\mathcal{S}_{1,2}(q_\|,\,\omega)]$ peak in the inset $(i4)$, giving rise to a profile for the total $\mathrm{Im}[\mathcal{S}(q_\|,\,\omega)]$ peak. As $q_\|/k_F = 0.1$, the defect-induced peak shift in $\delta\mathrm{Im}[\mathcal{S}_{1,1}(q_\|,\,\omega)]$ to lower ω can be seen from Fig. 7(b) but not for $\delta\mathrm{Im}[\mathcal{S}_{1,2}(q_\|,\,\omega)]$ in Fig. 7(d) except for a significant enhancement of the shoulder peak with increasing κ by interlayer Coulomb coupling. Moreover, by comparing Figs. 7(a) with 7(b), we find both $\mathrm{Im}[\mathcal{S}_{1,1}(q_\|,\,\omega)]$ and $\delta\mathrm{Im}[\mathcal{S}_{1,1}(q_\|,\,\omega)]$ are dominated by the intralayer Coulomb coupling $\mathcal{V}_{m,m';n,n'}(q_\|)$ given by Eq. (5).

C. Effects on Loss of Photons

In Sec. II B, the defect effects on the energy loss of electron beams in a multi-quantum-well system was discussed. As a comparison, the defect effects on the loss of photons (or photon absorption) in the same system will be investigated here. In this case, both the absorption coefficients for intrasubband and intersubband optical transitions of electrons can be calculated from [41]

$$\beta_{abs}(\omega) = \frac{\epsilon_d\,\omega}{n_r(\omega)c}\left[1 + \frac{1}{\exp(\hbar\omega/k_BT) - 1}\right]\mathrm{Im}\{\alpha_L(\omega)\}\ , \tag{33}$$

where $\hbar\omega$ is the incident-photon energy, and the dynamical refractive-index function $n_r(\omega)$ is

$$n_r(\omega) = \sqrt{\frac{\epsilon_d}{2}}\left\{1 + \mathrm{Re}\{\alpha_L(\omega)\} + \sqrt{[1 + \mathrm{Re}\{\alpha_L(\omega)]^2 + [\mathrm{Im}\{\alpha_L(\omega)]^2}\right\}^{1/2}\ . \tag{34}$$

For intrasubband transitions with an optical probe field polarized parallel to the quantum-well planes, $\alpha_L(\omega)$ in Eqs. (33) and (34) is the Lorentz ratio calculated as [12]

$$\alpha_L(\omega) = \alpha_L^{\parallel}(\omega) = -\left(\frac{2e^2}{\epsilon_0\epsilon_d L_W}\right)\pi\mathcal{R}_0^2 \sum_{j=0}^{N} \int \frac{d^2\mathbf{q}_\parallel}{(2\pi)^2}\, e^{-q_\parallel^2\mathcal{R}_0^2/4}\, \mathcal{Q}_j^{\parallel}(q_\parallel,\,\omega)\ , \tag{35}$$

where $\mathcal{R}_0$ is the radius of a normally-incident Gaussian light beam, $N+1$ is the total number of quantum wells in the system, and the optical-response function [42] $\mathcal{Q}_j^{\parallel}(q_\parallel,\,\omega)$ for the jth well is found to be

$$\mathcal{Q}_j^{\parallel}(q_\parallel,\,\omega) = \sum_n \tilde{\chi}_{n,n}(j,j|q_\parallel,\omega)\left(\frac{\hbar q_\parallel}{\mu^*\omega}\right)^2\ . \tag{36}$$

By including the couping due to interlayer Coulomb interactions, the partial polarization function $\tilde{\chi}_{n,n}(j,j';\,q_\parallel,\omega)$ introduced in Eq. (36) with $j=j'$ needs to be computed from the following self-consistent equations [36] (taking $n=n'$ and $j=j'$ afterwards), i.e.,

$$\tilde{\chi}_{n,n'}(j,j'|q_\parallel,\omega) = \chi_{n,n'}(q_\parallel,\,\omega)\,\delta_{j,j'} + \chi_{n,n'}(q_\parallel,\,\omega)\sum_{j''(\neq j)=0}^{N} V_c(ja,j''a|q_\parallel)\,\tilde{\chi}_{n,n'}(j'',j'|q_\parallel,\omega)\ , \tag{37}$$

where $\chi_{n,n'}(q_\parallel,\,\omega) \equiv \tilde{\chi}_{n,n'}(j,j|q_\parallel,\omega)$, and the interlayer Coulomb matrix elements $V_c(ja,j''a|q_\parallel)$ are still found from Eq. (19). By further taking into account the coupling between different subbands in each quantum well, the screened partial polarization function $\chi_{n,n'}(q_\parallel,\,\omega)$ in Eq. (37) must be calculated from Eq. (1) after finding the inverse dielectric function from Eqs. (3) and (4).

On the other hand, for a spatially-uniform optical probe field polarized perpendicular to the quantum-well planes, the Lorentz ratio $\alpha_L(\omega)$ in Eqs. (33) and (34) for intersubband transitions becomes [12]

$$\alpha_L(\omega) = \alpha_L^{\perp}(\omega) = -\frac{2e^2}{\epsilon_0\epsilon_d L_W}\sum_{j=0}^{N}\mathcal{Q}_j^{\perp}(q_\parallel=0,\,\omega)\ , \tag{38}$$

where we have assumed $q_\parallel/k_F = \sqrt{\epsilon_d}\,\omega/k_F c \ll 1$, and k_F is the Fermi wavenumber of electrons in quantum wells. In this case, the optical-response function for the jth well in Eq. (38) takes the form [42]

$$\mathcal{Q}_j^{\perp}(q_\parallel,\,\omega) = \sum_{n<n'}\tilde{\chi}_{n,n'}(j,j|q_\parallel,\omega)\left|\int_{-\infty}^{\infty}dz\,\mathcal{F}_{n'}(z)\,z\,\mathcal{F}_n(z)\right|^2\ . \tag{39}$$

Moreover, the influence of interlayer Coulomb coupling on the intersubband partial polarization function $\tilde{\chi}_{n,n'}(j,j'|q_\|,\omega)$ should still be determined from Eq. (37) (setting $j = j'$ afterwards).

A periodic stack of graphene layers embedded within a dielectric bulk is expected to have the properties of a one-dimensional photonic crystal with stop bands at certain frequencies. As an incident electromagnetic wave is reflected from these stacked graphene layers, the tuning of the graphene Fermi energy or conductivity renders the possibility of controlling these stop bands, leading to a tunable spectral-selective mirror. [43] In addition, a transfer-matrix method was applied to explore optical reflection, transmission and absorption in single-, double- and multi-layer graphene structures. [44] Both the total internal reflection in single-layer graphene, as well as thin-film interference effects in double-layer graphene, are shown for increasing light absorption.

For intrasubband electron transitions induced by an optical field with a polarization parallel to the quantum-well plane, we present in Fig. 8(a) the defect modification to the absorption coefficient $\delta\beta^{\|}_{abs}(\omega)$ calculated from Eqs. (33) and (35). Here, the low-energy photon absorption peak in the inset $(i1)$ is attributed to the excitation of intrasubband plasmons, and this peak is shifted to an even lower ω value with increasing κ. On the other hand, for the intersubband transition of electrons under an optical field polarized perpendicular to the quantum-well plane, we display in Fig. 8(b) the defect changes in absorption coefficient $\delta\beta^{\perp}_{abs}(\omega)$ calculated from Eqs. (33) and (38). In this case, however, a high-energy and broad photon absorption peak in the inset $(i2)$ results from intrasubband-plasmon excitations, and no shift associated with this peak with κ is found.

As displayed in Figs. 8(a) and 8(b), the reductions by proton-induced defects in both $\delta\beta^{\|}_{abs}(\omega)$ for intraband absorption and $\delta\beta^{\perp}_{abs}(\omega)$ for interband absorption will give rise to a decreased photo-responsivity [28, 29] of quantum-well infrared detectors. As a consequence of this reduction, the lifetime of satellite onboard electronic and optoelectronic devices will be shortened greatly. Therefore, the current theory can lead to a more realistic characterization of quantum-well photodetectors not only for high quantum efficiency and low dark current density [28, 29] but also for radiation tolerance or ability to withstand the effects of the radiation they will experience in a particular orbit.

III. ULTRAFAST POINT-DEFECT DYNAMICS

In Sec. II, we only discuss the effects of point defects on losses of electron energy and photons in a multi-quantum-well system. In Sec. III, we explore ultrafast dynamics for the production of Frenkel-pair defects and their follow-up reactions and diffusions in the same system. In this way, the spatial dependence of the one-dimensional distribution function $\rho_d(z)$ introduced in Eq. (7) for the defect-electron interaction can be extracted. It is known that the Frenkel-pair production will be followed subsequently by diffusion and reactions to reach defect stabilization through diffusion-induced recombination and reactions with residual defects in the system. Here, the diffusion of point defects is driven by forces other than the concentration gradient of defects, e.g., compressive stress near sinks. The reactions, on the other hand, are enabled by the presence of growth-induced dislocation loops at the two interfaces of a quantum well.

A. Defect Diffusion-Reaction Equations

Let us start by considering an N layered material structure in the z direction. Each material layer is characterized by the (bulk) irradiation parameters $\mathcal{G}_0^j$, $\mathcal{R}^j$, D^j and $\Gamma^j(t)$ with layer labels $j = 1, 2, 3, \cdots, N$ for production and recombination rates, diffusion coefficient and bulk-sink annihilation, respectively. In modeling a mesoscopic-scale sample, the interface-sink strengths $[\kappa^j(t)]^2$ with $j = 1, 2, 3, \cdots, N-1$ also need to be taken into account.

For a reaction-rate control system, we can write down the diffusion-reaction equations [1] for the concentrations of point vacancies and interstitial atoms as

$$\begin{aligned}
&\frac{\partial c_v^j(z,t)}{\partial t} - D_v^j\,\frac{\partial^2 c_v^j(z,t)}{\partial z^2} = \mathcal{G}_0^j - \frac{\mathcal{B}_{iv}^j\,\Omega_j(D_i^j + D_v^j)}{(a_0^j)^2}\,c_i^j(z,t)\,c_v^j(z,t)\\
&- \sum_{\ell=4}^{\infty} \frac{\mathcal{B}_v^{j+1} D_v^{j+1} a_0^{j+1}}{1-(\mathcal{B}_v^{j+1}/2\pi)\ln\{\pi[R_{vd}^{j+1}(\ell)]^2\sigma_{dl}^{j+1}(\ell,t)\}}\,\sigma_{dl}^{j+1}(\ell,t)\,c_v^{j+1}(z,t)\,\delta(z-z_{j+1})\\
&- \sum_{\ell=4}^{\infty} \frac{\mathcal{B}_v^{j} D_v^{j} a_0^{j}}{1-(\mathcal{B}_v^{j}/2\pi)\ln\{\pi[R_{vd}^{j}(\ell)]^2\sigma_{dl}^{j}(\ell,t)\}}\,\sigma_{dl}^{j}(\ell,t)\,c_v^{j}(z,t)\,\delta(z-z_{j})\ ,
\end{aligned} \tag{40}$$

$$
\begin{aligned}
&\frac{\partial c_i^j(z,t)}{\partial t} - D_i^j\,\frac{\partial^2 c_i^j(z,t)}{\partial z^2} = \mathcal{G}_0^j - \frac{\mathcal{B}_{iv}^j\,\Omega_j(D_i^j + D_v^j)}{(a_0^j)^2}\,c_i^j(z,t)\,c_v^j(z,t)\\
&- \sum_{\ell=4}^{\infty}\frac{\mathcal{B}_i^{j+1}D_i^{j+1}a_0^{j+1}}{1-(\mathcal{B}_i^{j+1}/2\pi)\ln\{\pi[R_{id}^{j+1}(\ell)]^2\sigma_{dl}^{j+1}(\ell,t)\}}\,\sigma_{dl}^{j+1}(\ell,t)\,c_i^{j+1}(z,t)\,\delta(z-z_{j+1})\\
&- \sum_{\ell=4}^{\infty}\left\{\frac{\mathcal{B}_i^j D_i^j a_0^j}{1-(\mathcal{B}_i^j/2\pi)\ln\{[\pi[R_{id}^j(\ell)]^2\sigma_{dl}^j(\ell,t)\}}\right\}\sigma_{dl}^j(\ell,t)\,c_i^j(z,t)\,\delta(z-z_j)\ , \qquad (41)
\end{aligned}
$$

where the small thermal-equilibrium concentration of point vacancies has been neglected at low temperatures, $\mathcal{B}_{iv}^j$ is the bias factor for recombinations [1], $\mathcal{B}_v^j \neq \mathcal{B}_i^j$ are the bias factors for vacancies (v) and interstitials (i), and D_v^j and D_i^j are the diffusion coefficients. The terms on the right-hand side of the equations correspond to diffusion sources and reactions, integer j is the layer index, integer ℓ indicates the number of interstitials enclosed within a planar dislocation loop [45], z_j and z_{j+1} represent the left and right interface positions of the jth layer, $c_v^j(z,t)$ and $c_i^j(z,t)$ are the concentrations of point vacancies and interstitials, and $\mathcal{G}_0^j$ is the production rate for Frenkel pairs. Here, $\rho_d(z)$ can be obtained by multiplying the sample cross-sectional area with $c_v^j(z,t)$ and $c_i^j(z,t)$. In addition, in Eqs. (40) and (41), we used the facts that in a reaction-rate control system $\mathcal{R}^j \equiv \Gamma_{i,v}^j = \mathcal{B}_{iv}^j\,\Omega_j D_{i,v}^j/(a_0^j)^2$ for the vacancy-interstitial recombination rate, $\Gamma_{\{i,v\}d}^j(\ell,t) = [\kappa_{\{i,v\}d}^j(\ell,t)]^2 D_{\{i,v\}}^j/\sigma_{dl}^j(\ell,t)$ is the rate for the interaction between defects and interface dislocation loops, and $[\kappa_{\{i,v\}d}^j(\ell,t)]^2 = \mathcal{B}_{\{i,v\}d}^j(\ell)\,\sigma_{dl}^j(\ell,t)$ for the dislocation loop-sink strength, where Ω_j is the atomic volume, a_0^j is the lattice constant, and $c_{FP}^j = \sqrt{\mathcal{G}_0^j(a_0^j)^2/[\mathcal{B}_{iv}^j\Omega_j(D_i^j + D_v^j)]}$ is the initial number of Frenkel pairs. Furthermore, $\mathcal{B}_{\{i,v\}d}^j(\ell) \sim \mathcal{B}_{i,v}^j$ and $R_{\{i,v\}d}^j(\ell) \sim \ell a_0^j/2\pi$ are the bias factors for the reactions and the capture radii of vacancy-dislocation loop (vd) and interstitial-dislocation loop (id), and finally $\sigma_{dl}^j(\ell,t)$ is the growth-strain-induced interface dislocation-loop (enclosing ℓ captured interstitial atoms) areal density.

The diffusion coefficients $D_{i,v}^j$ for point vacancies and interstitials can be calculated from [1]

$$
D_{i,v}^j = \alpha^j\,(a_0^j)^2\,\omega_D^j\,\exp\left(-\frac{E_{i,v}^j}{k_BT}\right)\ , \qquad (42)
$$

where $E_{i,v}^j$ are the migration energies for point vacancies and interstitials, α^j is determined by the diffusion mechanism and crystal symmetry, $\omega_D^j = (6\pi^2/\Omega_j)^{1/3}\,v_s$ is the Debye frequency and v_s is the sound velocity of the host semiconductor.

The interface dislocation-loop density $\sigma^j_{dl}(\ell,t)$ in Eqs. (40) and (41) can be found from the following reaction equation [1] (for $\ell \geq 4$), i.e.

$$\frac{\partial \sigma^j_{dl}(\ell,t)}{\partial t} = \left[\beta^j_v(\ell+1,t)+\alpha^j_i(\ell+1,t)\right]\sigma^j_{dl}(\ell+1,t)+\beta^j_i(\ell-1,t)\,\sigma^j_{dl}(\ell-1,t)$$

$$-\left[\beta^j_v(\ell,t)+\beta^j_i(\ell,t)+\alpha^j_i(\ell,t)\right]\sigma^j_{dl}(\ell,t)\ , \tag{43}$$

where $\sigma^j_{dl}(\ell,t=0)=\sigma^j_0\,\delta_{\ell,4}$ and σ^j_0 is the initial density for the smallest interface dislocation loops containing four interstitials, the absorption $[\beta^j_{i,v}(\ell,t)]$ and the emission $[\alpha^j_i(\ell,t)]$ rates are given by [1]

$$\beta^j_{i,v}(\ell,t)=\ell a^j_0\,\mathcal{B}^j_{i,v}\,D^j_{i,v}\,c^j_{i,v}(z_j,t)\ , \tag{44}$$

$$\alpha^j_i(\ell,t)=\ell a^j_0\,\mathcal{B}^j_i\left(\frac{D^j_i}{\Omega_j}\right)\exp\left[-\frac{E^j_{b,i}(\ell)}{k_BT}\right]\ , \tag{45}$$

and $E^j_{b,v}(\ell)$ is the binding energy for a planar cluster of ℓ interstitials.

We show in Figs. 9(a) and 9(c) the steady-state spatial distributions for concentrations of point vacancies $c^j_v(z)$ and interstitials $c^j_i(z)$ in an AlAs/InAs/GaAs single-quantum-well system. We notice from Eqs. (40), (41) and (43) that both $c^j_v(z)$ and $c^j_i(z)$ in a steady state eventually become proportional to $\mathcal{G}^j_0$ although c^j_{FP} is initially proportional to $\sqrt{\mathcal{G}^j_0}$. Here, the comparison of results at $T=400\,\mathrm{K}$ (upper) and $300\,\mathrm{K}$ (lower) are presented to demonstrate the diffusion of point vacancies into the well through both interfaces due to thermally-enhanced diffusion coefficients of vacancies. However, the interstitial concentration around the left interface is greatly depleted (deep dip) at $T=400\,\mathrm{K}$ as a result of large absorptions by dislocation loops although they still diffuse into the well through the right interface. In Figs. 9(b) and 9(d), we display results for steady-state distributions of dislocation-loop densities $\sigma^j_{dl}(\ell)$ ($\ell \geq 4$) as functions of loop-site number, corresponding to the left ($j=1$) and right ($j=2$) interfaces at $T=300$ and $400\,\mathrm{K}$. Here, the increases of dislocation-loop densities ($\ell=4$) at the left interface and the simultaneous swellings of dislocation loops ($\ell>4$) at the right interface are found due to the enhanced reactions with point interstitials by their increased diffusion coefficients. Moreover, the defect diffusions occur mainly around interfaces between two adjacent layers or across the interfaces, and

$c_v^j(z) \neq c_i^j(z)$ due to their different diffusion coefficients although these two concentrations are initially identical.

If the penetration depth of protons is larger than the sample thickness, the overall distribution of defects for a multiple-quantum-well structure can be determined by repeating the single-well defect distribution along the growth direction. Therefore, our defect diffusion-reaction model for the AlAs/InAs/GaAs quantum well is adequate for the multi-quantum-well system.

B. Defect Production by Proton Radiation

The diffusion-reaction equations presented in Sec. III A can be applied to find the spatial dependence of the one-dimensional distribution function $\rho_d(z)$ of defects. However, the initial conditions of these equations require the production rate and the concentration of proton-produced Frenkel pairs. Therefore, we must study the production dynamics of point defects under proton irradiation with different kinetic energies, which connects the lab-measured defect effects ($\propto$ number of point defects) to space-measured energy-dependent proton fluxes in a particular earth orbit. For this purpose, an atomic-level molecular-dynamics simulation approach is employed with help from a Tersoff potential fitted by parameters. [46, 47]

For a bulk material, the production rate per unit volume $\mathcal{G}_0(E_i)$ [$\text{sec}^{-1}\cdot\text{cm}^{-3}$] for the displacement atoms in a crystal lattice can be calculated from [1]

$$\mathcal{G}_0(E_i) = n_{at}\,\sigma_D(E_i)\,\mathcal{F}_0(E_i)\ , \tag{46}$$

where E_i [MeV] is the incident proton kinetic energy, n_{at} [cm^{-3}] is the crystal atom volume density, $\mathcal{F}_0(E_i)$ [$\text{cm}^{-2}\cdot\text{sec}^{-1}$] is the incident energy-dependent proton flux, and $\sigma_D(E_i)$ [cm^2] is the energy-dependent displacement cross section.

Physically, the displacement cross section $\sigma_D(E_i)$ in Eq. (46) describes the probability for the displacement of struck lattice atoms by incident protons, therefore, we can directly write

$$\sigma_D(E_i) = \int\limits_{E_d}^{\varepsilon_{max}(E_i)} d\varepsilon_T\ \mathcal{Q}(\varepsilon_T)\,\sigma_C(E_i,\varepsilon_T)\,\mathcal{N}_{MD}(\varepsilon_T)\ , \tag{47}$$

where $\sigma_C(E_i, \varepsilon_T)$ [$\mathrm{cm}^2 \cdot (\mathrm{keV})^{-1}$] is the differential energy transfer cross section by collision with the lattice, which measures the probability that an incident proton with kinetic energy E_i will transfer a recoil energy ε_T [keV] to a struck lattice atom, $\mathcal{N}_{MD}(\varepsilon_T)$ [no unit] represents the average number of displaced atoms produced by collision with the lattice, and E_d labels the energy threshold, i.e., the energy required to produce a stable Frenkel pair. In addition, $\varepsilon_{max}(E_i) = [4m_0M_0/(m_0+M_0)^2]\,E_i$ is the upper limit for the recoil energy gained by the struck lattice atom, where M_0 refers to the mass of lattice atoms and m_0 to the mass of incident protons.

The function $\mathcal{Q}(\varepsilon_T)$ [dimensionless] introduced in Eq. (47) is the so-called Lindhard partition function and is written as [48–50]

$$\mathcal{Q}(\varepsilon_T) = \frac{1}{1 + \mathcal{K}_L\, g(\varepsilon_T/E_L)} \ , \tag{48}$$

where the Ziegler-Biersack-Littmark (ZBL) reduced-energy E_L is defined as

$$E_L = \left(\frac{m_0 + M_0}{M_0}\right) \frac{Z_1 Z_2 e^2}{4\pi\epsilon_0 a_u} \ , \tag{49}$$

while the reduced electronic energy-loss factor $\mathcal{K}_L$ is

$$\mathcal{K}_L = \frac{Z_1^{2/3} Z_2^{1/2}}{12.6\left(Z_1^{2/3} + Z_2^{2/3}\right)^{3/4}} \frac{[(1 + (M_0/m_0)]^{3/2}}{\sqrt{M_0/m_0}} \ , \tag{50}$$

$m_0 = 1.67 \times 10^{-27}\,\mathrm{kg}$ is the proton mass, $a_u = 0.8853\, a_B / \left(Z_1^{2/3} + Z_2^{2/3}\right)^{1/2}$ is the ZBL universal screening length, $a_B = 4\pi\epsilon_0\hbar^2/m_e e^2 = 0.5292\,\text{Å}$ is the Bohr radius, m_e is the free-electron mass, and the Lindhard function $g(x)$ is calculated as

$$g(x) = x + 0.40244\, x^{3/4} + 3.4008\, x^{1/6} \ . \tag{51}$$

In the current case, we set $Z_1 = 1$ (proton), $Z_2 = 31$ (Ga) or 33 (As) for the nuclear charge number of lattice atoms.

Moreover, the differential energy transfer cross section $\sigma_C(E_i, \varepsilon_T)$ [$\mathrm{cm}^2 \cdot (\mathrm{keV})^{-1}$] can be approximated as [50]

$$\sigma_C(E_i, \varepsilon_T) = -\frac{\pi a_u^2}{2}\, \alpha_s^2(E_i)\, \frac{h_0([\tau(E_i, \varepsilon_T)]^{1/2})}{[\tau(E_i, \varepsilon_T)]^{3/2}\, \varepsilon_{max}(E_i)} \ , \tag{52}$$

where $\tau(E_i,\varepsilon_T) = \alpha_s^2(E_i)\varepsilon_T/\varepsilon_{max}(E_i)$ is the dimensionless collision parameter, $\alpha_s(E_i) = E_i/E_L$ is the scaled ZBL reduced energy. The function $h_0(x)$ introduced in Eq. (52) is defined as

$$h_0(x) = \frac{\ln A(x)}{2B(x)} + \frac{ax}{2A(x)B(x)} - \frac{x\ln A(x)\left(1+bc\,x^{c-1}+d/2x^{1/2}\right)}{2B^2(x)}\ , \tag{53}$$

where $A(x) = 1+ax$, $B(x) = x+bx^c+dx^{1/2}$, $a = 1.1383$, $b = 0.01321$, $c = 0.21226$ and $d = 0.19593$ are four parameters.

Finally, $\mathcal{N}_{MD}(\varepsilon_T)$ in Eq. (47) can be computed by using MD simulations. As shown in Fig. 10, the calculated $\mathcal{N}_{MD}(\varepsilon_T)$ can be fitted reasonably well by a simple power law, i.e., $\mathcal{N}_{MD}(\varepsilon_T) = \mathcal{A}_0[\varepsilon_T(\text{keV})]^n$ with proper fitting parameters $\mathcal{A}_0$ and n. Finally, by combining together the results in Eqs. (46)-(52), for a given flux spectrum $\mathcal{F}_0(E_i)$ we get the production rate $\mathcal{G}_0(E_i)$ per unit volume as

$$\mathcal{G}_0(E_i) = -\frac{n_{at}\pi a_u^2\mathcal{A}_0}{2}\left[\frac{\alpha_s^2(E_i)\mathcal{F}_0(E_i)}{\varepsilon_{max}(E_i)}\right]$$
$$\times\int\limits_{E_d}^{\varepsilon_{max}(E_i)} d\varepsilon_T\,\mathcal{Q}(\varepsilon_T)\,[\varepsilon_T(\text{keV})]^n\,\frac{h_0([\tau(E_i,\varepsilon_T)]^{1/2})}{[\tau(E_i,\varepsilon_T)]^{3/2}}\ , \tag{54}$$

which can be evaluated numerically once fitting parameters $\mathcal{A}_0$ and n are obtained. Here, $\mathcal{G}_0(E_i)$ is related to the more familiar non-ionizing energy loss [22] NIEL(E_i) by $\mathcal{G}_0(E_i) = (\rho_{at}/n_{at})\,(0.4/E_d)\,\mathcal{F}_0(E_i)\,\text{NIEL}(E_i)$ with ρ_{at} being a crystal atom weight density. [22] Furthermore, the concentration $c_{FP}(E_i)$ for Frenkel-pair defects can be roughly estimated from $c_{FP}(E_i) = \mathcal{G}_0(E_i)\,(\tau_0+\tau_t/2)$, where τ_t is the effective proton transit time through the sample, and $\tau_0 \sim 10\,\text{ns}$, which is proportional to $1/\sqrt{\mathcal{F}_0(E_i)}$, is the time required to reach a steady state for generation of Frenkel-pair defects after the production has been balanced by the recombination.

We present in Fig. 11 the numerical results for calculated number of lattice-atom displacements as a function of time after a Ga PKA has been introduced to a GaAs crystal with the recoil energy $\varepsilon_T = 10\,\text{keV}$. From Fig. 11, we find that the number of lattice-atom displacements reaches a peak value N_{pk} at about $t = 0.8\,\text{ps}$. After this peak time, only 13% of the displaced atoms recombine with vacancies, and most anti-site defects are generated during the collisional phase. In addition, a steady state with $\varepsilon_T = 10\,\text{keV}$ has been reached for $t > 10\,\mathrm{ps}$, where As defects are slightly higher than that of Ga defects due to the smaller formation energy for As defects [23].

The numerical results for the number $\mathcal{N}_F(\varepsilon_T)$ of Ga and As displaced atoms and anti-site defects as a function of recoil energy ε_T at $t = 10\,\mathrm{ps}$ are displayed in Fig. 12, where the NRT result is given by $\mathcal{N}_F(\varepsilon_T) = N_{NRT}(\varepsilon_T) \equiv 0.8\,\varepsilon_T/2E_d$. It is clear from this figure that the number of defects in steady state is found to be much high than that given by the NRT value. Moreover, nonlinear dependence on ε_T is limited only for low-energy PKA recoils.

In order to provide initial Frenkel-pair defect concentrations and its production rate, we show in Fig. 13 the numerical result of Eq. (54) for $\mathcal{G}_0(E_i)$. It is clear from this figure that there exists a peak for $\mathcal{G}_0(E_i)$ as a function of incident proton kinetic energy due to competition between increasing $\varepsilon_{max}(E_i)$ and decreasing $\sigma_C(E_i, \varepsilon_T)$ at the same time.

IV. SUMMARY AND REMARKS

In conclusion, we have investigated the effects of point defects on the loss of either electron kinetic energy or incident photons in a multi-quantum-well system. The influence of proton-radiation-produced defects is taken into account by applying the vertex correction to a bare polarization function of electrons in quantum wells within the ladder approximation, which goes beyond the usual second-order Born approximation. Both intralayer and interlayer dynamical screenings to the defect-electron interaction have also been considered under the random-phase approximation. Furthermore, the defect effects on the electron-energy loss function, as well as on intrasubband and intersubband optical absorption, have been shown and discussed.

To find the distribution function of point defects in a layered structure for calculations of defect effects, we have applied the diffusion-reaction-equation method, where the reactions of point defects with the growth-induced dislocation loops on interfaces of the multi-layered system have been included, and the increase and decrease of dislocation-loop density and point-defect concentrations were found at the same time due to thermal enhancement of defect diffusion. In addition, the Frenkel-pair defect production rate and the initial concentration of Frenkel pairs were obtained from an atomic-level molecular-dynamics model after fitting the numerical results for Frenkel pairs as a function of energy of a primary knock-on atom.

The defect effect, diffusion-reaction and molecular dynamics models presented in this paper can be combined with a space-weather forecast model [20, 21] which predicts spatial-temporal fluxes and particle velocity distributions. In addition, the atomic-level molecular dynamics model employed in this paper is based on a fitted short- and long-range interaction among all atoms from extensive calculations using the first-principle density-functional theory for an individually considered material. With this combination of theories, the predicted irradiation conditions for particular satellite orbits allow electronic and optoelectronic devices to be specifically designed for operation in space with radiation-hardening considerations [17] (such as self-healing and mitigation). This approach will effectively extend the lifetime of satellite onboard electronic and optoelectronic devices in non-benign orbits and greatly reduce the cost. The theory in this paper can be applied to space-based sensing and imaging, and leads to a more realistic characterization of quantum-well photodetectors not only for high quantum efficiency and low dark current density but also for radiation tolerance or mitigating the effects of the radiation.

Acknowledgments

This material is based upon work supported by the Air Force Office of Scientific Research (AFOSR). We would also like to thank Dr. Paul D. LeVan and Dr. Sanjay Krishna for their helpful discussions.

[1] G. S. Was, *Fundamentals of Radiation Materials Science: Metals and Alloys* (Springer-Verlag, Berlin, Heidelberg, 2007).

[2] P. Sigmund, *Particle Penetration and Radiation Effects* (Springer-Verlag, Berlin, Heidelberg, 2006).

[3] K. Nordlund, J. Peltola, J. Nord, J. Keinonen, and R. S. Averback, Defect clustering during ion irradiation of GaAs: Insight from molecular dynamics simulations, J. Appl. Phys. **90**, 1710 (2001).

[4] R. Devanathan, W. J. Weber, and F. Gao, Atomic scale simulation of defect production in irradiated 3C-SiC, J. Appl. Phys. **90**, 2303 (2001).

[5] M. Posselt, F. Gao, and D. Zwicker, Atomistic study of the migration of di- and tri-interstitials in silicon, Phys. Rev. B **71**, 245202 (2005).

[6] F. Gao and W. J. Weber, Recovery of close Frenkel pairs produced by low energy recoils in SiC, J. Appl. Phys. **94**, 4348 (2003).

[7] F. Gao, H. Xiao, X. Zu, M. Posselt, and W. J. Weber, Defect-Enhanced Charge Transfer by Ion-Solid Interactions in SiC using Large-Scale Ab Initio Molecular Dynamics Simulations, Phys. Rev. Lett. **103**, 027405 (2009).

[8] Z. Rong, F. Gao, and W. J. Weber, Monte Carlo simulations of defect recovery within a 10 keV collision cascade in 3C-SiC, J. Appl. Phys. **102**, 103508 (2007).

[9] L. A. Maksimov and A. I. Ryazanov, Kinetic equation for vacancion pores. The pore lattice as a dissipative structure, stable under irradiation conditions, Sov. Phys. JETP **52**, 1170 (1980).

[10] S. I. Golubov, A. V. Barashev, and R. E. Stoller, *Comprehensive Nuclear Materials*, edited by R. Konings, R. Stoller, T. Allen, and S. Yamanaka (Elsevier Ltd., Amsterdam, 2012), ch. 13.

[11] G. Gumbs and D. H. Huang, *Properties of Interacting Low-Dimensional Systems* (Wiley-VCH Verlag GmbH & Co. KGaA, Boschstr, Weinheim, 2011).

[12] D. H. Huang and M. O. Manasreh, Intersubband transitions in strained $In_{0.07}Ga_{0.93}As/Al_{0.40}Ga_{0.60}As$ multiple quantum wells and their application to a two-colors photodetector, Phys. Rev. B **54**, 5620 (1996).

[13] T. Ando, A. B. Fowler and F. Stern, Electronic properties of two-dimensional systems, Rev. Mod. Phys. **54**, 437 (1982).

[14] G. Gumbs, D. H. Huang, Y. Yin, H. Qiang, D. Yan, F. H. Pollak, and T. F. Noble, Many-body effects in the electromodulation spectra of modulation-doped quantum wells: Theory and experiment, Phys. Rev. B **48**, 18328 (1993).

[15] A. Hallén, D. Fenyö, B. U. R. Sundqvist, R. E. Johnson, and B. G. Sevensson, The influence of ion flux on defect production in MeV protonirradiated silicon, J. Appl. Phys. **70**, 3025 (1991).

[16] N. V. Doan and G. Martin, Elimination of irradiation point defects in crystalline solids: Sink strengths, Phys. Rev. B **67**, 134107 (2003).

[17] D. H. Huang, F. Gao, D. A. Cardimona, C. P. Morath, and V. M. Cowan, Multi-timescale theory for radiation degradation of electronic and optoelectronic devices, Am. J. Space Sci. **3**,

3 (2015).

[18] C. Claeys and E. Simoen, *Radiation Effects in Advanced Semiconductor Materials and Devices* (Springer, 2002).

[19] J. E. Hubbs, P. W. Marshall, C. J. Marshall, M. E. Gramer, D. Maestas, J. P. Garcia, G. A. Dole, and A. A. Anderson, Lateral Diffusion Length Changes in HgCdTe Detectors in a Proton Environment, IEEE Trans. Nucl. Sci. **54**, 2435 (2007).

[20] M. Moldwin, *An Introduction to Space Weather* (Cambridge University Press, New York, 2008).

[21] D. L. Cooke and I. Katz, Ionization-induced instability in an electron-collecting sheath, J. Spacecraft and Rockets, **25**, 132 (1988).

[22] F. Gao, N. J. Chen, E. Hernandez-Rivera, D. H. Huang, and P. D. LeVan, Displacement damage as revealed by computer simulations and effective non-ionizing energy loss in GaAs, J. Appl. Phys. **121**, 095104 (2017).

[23] N. J. Chen, S. Gray, E. Hernandez-Rivera, D. H. Huang, P. D. LeVan, and F. Gao, Computational simulation of threshold displacement energies of GaAs, J. Materials Research **32**, 1555 (2017).

[24] V. M. Cowan, C. P. Morath, J. E. Hubbs, S. Myers, E. Plis and S. Krishna, Radiation tolerance characterization of dual band InAs/GaSb type-II strain-layer superlattice pBp detectors using 63 MeV protons, Appl. Phys. Lett. **101**, 251108 (2012).

[25] C. P. Morath, V. M. Cowan, L. A. Treider, G. Jenkins and J. E. Hubbs, Proton Irradiation Effects on the Performance of III-V-Based, Unipolar Barrier Infrared Detectors, IEEE Trans. Nucl. Sci. **62**, 512 (2015).

[26] B. F. Levine, Quantum-well infrared photodetectors, J. Appl. Phys. **74**, R1 (1993).

[27] A. Rogalski, Quantum well photoconductors in infrared detector technology, J. Appl. Phys. **93**, 4355 (2003).

[28] D. H. Huang and D. A. Cardimona, Physics of non-adiabatic transport and field-domain effect in quantum-well infrared photodetectors, Infr. Phys. & Techn. **44**, 487 (2003).

[29] D. H. Huang, C. Morath, D. A. Cardimona, and A. Singh, Thermal hysteresis loop, dynamical breakdown, and emission-current spike in quantum-well photodetectors, J. Appl. Phys. **90**, 6032 (2001).

[30] D. H. Huang and S.-X. Zhou, Theoretical Investigation of Collective Excitations in HgTe-CdTe

Superlattices. I. Intrasubband Excitation, Phys. Rev. B **38**, 13061 (1988).

[31] D. H. Huang and S.-X. Zhou, Theoretical Investigation of Collective Excitations in HgTe-CdTe Superlattices. II. Intersubband Excitation and Effects of Magnetic Field and Electron-Phonon Coupling, Phys. Rev. B **38**, 13069 (1988).

[32] D. H. Huang, G. Gumbs and N. J. M. Horing, Magneto-Optical Absorption in an One-Dimensional Array of Narrow Antiwires, Phys. Rev. B **49**, 11463 (1994).

[33] D. H. Huang and M. O. Manasreh, Effects of the Screened Exchange Interaction on the Tunneling and Landau Gaps in Double Quantum Wells, Phys. Rev. B **54**, 2044 (1996).

[34] D. H. Huang, P. M. Alsing, T. Apostolova and D. A. Cardimona, Coupled energy-drift and force-balance equations for high-field hot-carrier transport, Phys. Rev. B **71**, 195205 (2005).

[35] F. J. García de Abajo, Optical excitations in electron microscopy, Rev. Mod. Phys. **82**, 209 (2010).

[36] G. Gumbs, Inelastic electron scattering from the surfaces of semiconductor multilayers: Study of subband structure within the quantum well, Phys. Rev. B **39**, 5186 (1989).

[37] G. Gumbs and N. J. M. Horing, Plasma losses by charged particles in thin films: Effects of spatial dispersion, phonons, and magnetic field, Phys. Rev. B **43**, 2119 (1991).

[38] B. N. J. Persson and E. Zaremba, Electron-hole pair production at metal surfaces, Phys. Rev. B **31**, 1863 (1985).

[39] A. Iurov, G. Gumbs, D. H. Huang and V. Silkin, Plasmon dissipation in gapped-graphene open systems at finite temperatures, Phys. Rev. B **93**, 035404 (2016).

[40] F. J. García de Abajo, Multiple Excitation of Confined Graphene Plasmons by Single Free Electrons, ACS Nano **7**, 11409 (2013).

[41] G. Gumbs, D. H. Huang, and D. N. Talwar, Doublet Structure in the Absorption Coefficient Between Tunneling Split Intersubband Transitions in Double Quantum Wells, Phys. Rev. B **53**, 15436 (1996).

[42] D. H. Huang, C. Rhodes, P. M. Alsing, and D. A. Cardimona, Effects of longitudinal field on transmitted near field in doped semi-infinite semiconductors with a surface conducting sheet, J. Appl. Phys. **100**, 113711 (2006).

[43] Yu. V. Bludov, N. M. R. Peres, and M. I. Vasilevskiy, Unusual reflection of electromagnetic radiation from a stack of graphene layers at oblique incidence, J. Opt. **15**, 114004 (2013).

[44] T. Zhan, X. Shi, Y. Dai, X. Liu, and J. Zi, Transfer matrix method for optics in graphene

layers, J. Phys.: Condens. Matt. **25**, 215301 (2013).

[45] R. Bullough, M. R. Hayns, and C. H. Woo, The sink strength of dislocation loops and their growth in irradiated materials, J. Nucl. Mater. **84**, 93 (1979).

[46] J. Tersoff, New empirical approach for the structure and energy of covalent systems, Phys. Rev. B **37**, 6991 (1988).

[47] F. Gao, and W. J. Weber, Atomic-scale simulation of 50 keV Si displacement cascades in β-SiC, Phys. Rev. B **63**, 054101 (2000).

[48] S. R. Messenger, E. A. Burke, M. A. Xapsos, G. P. Summers, R. J. Walters, I. Jun, and T. Jordan, NIEL for heavy ions: an analytical approach, IEEE Trans. Nucl. Sci. **50**, 1919 (2003).

[49] J. F. Ziegler, J. P. Biersack, and U. Littmark, *The Stopping and Range of Ions in Solids* (vol. I, Pergamon Press, New York, 1985).

[50] M. Nastasi, J. W. Mayer, and J. K. Hirvonen, Ion-Solid Interactions, *Fundamentals and Applications* (Cambridge Univ. Press, New York, 2004).

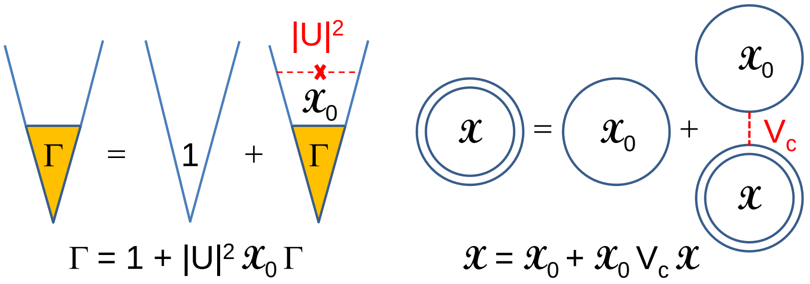

FIG. 1: (Left) Graphic representation for the ladder approximation used in Eq. (7); (Right) graphic representation for the random-phase approximation employed in Eq. (21).

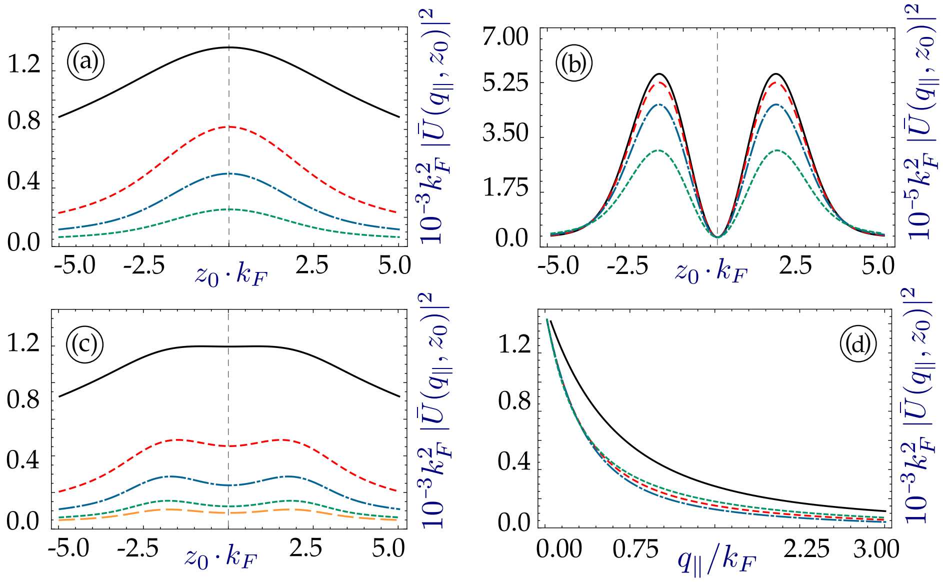

FIG. 2: $|U_{n,n'}(q_\parallel, z_0)|^2$ (in units of k_F^{-2}) as functions of $z_0 k_F$ in (a) for $|\overline{U}_{1,1}|^2$ and $q_\parallel / k_F = 0.1$ (black), 0.5 (red), 1.0 (blue), 2.0 (green); in (b) for $|\overline{U}_{1,2}|^2$ and $q_\parallel / k_F = 0.1$ (black), 1.0 (red), 2.0 (blue), 3.0 (green); in (c) for $|\overline{U}_{2,2}|^2$ and $q_\parallel / k_F = 0.1$ (black), 0.5 (red), 1.0 (blue), 2.0 (green), 3.0 (orange); as well as a function of $q_\parallel / k_F$ in (d) for $|\overline{U}_{1,1}|^2$, $k_F z_0 = 0.0$ (black) and 2.0 (red); for $|\overline{U}_{2,2}|^2$, $k_F z_0 = 0.0$ (blue) and 2.0 (green). Here, $k_F = \sqrt{2\pi n_{QW}}$ is the Fermi wave vector, $n_{QW} = 1.0 \times 10^{11}\,\mathrm{cm}^{-2}$ is the quantum-well doping density, $L_W = 100\,\mathrm{nm}$, $\mu^* = 0.067\, m_0$ with free-electron mass m_0, and $\Lambda_\parallel = 10\,\text{Å}$.

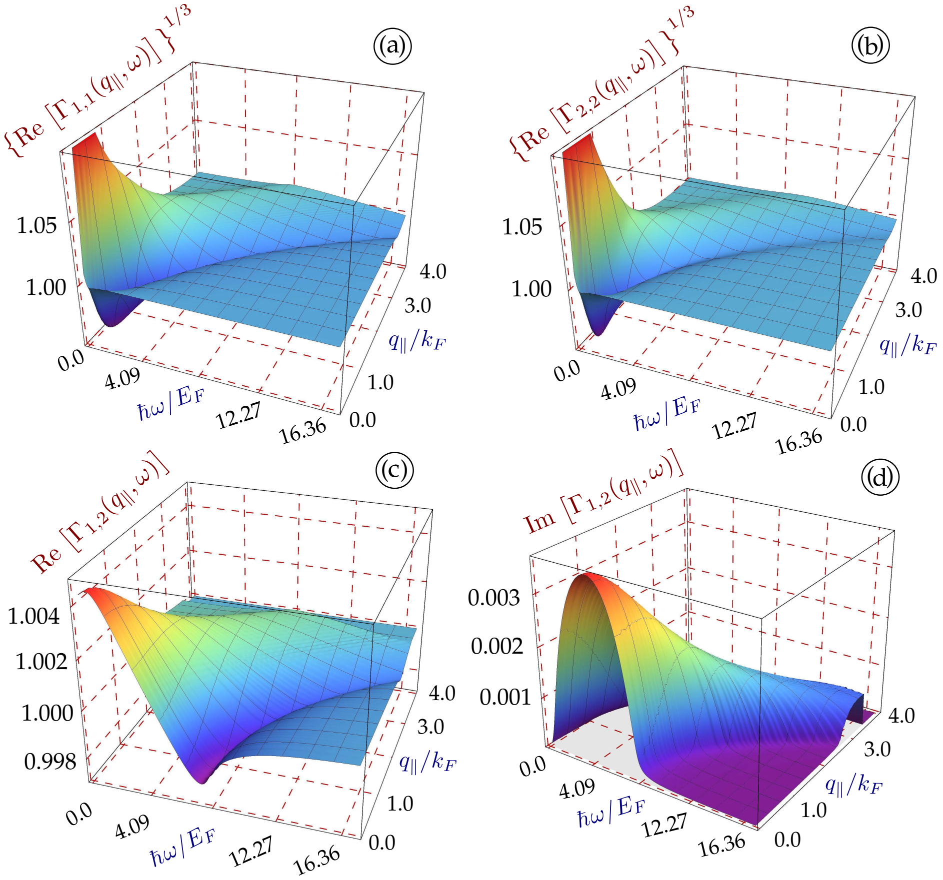

FIG. 3: 3D plots of dimensionless $\Gamma_{n,n'}(q_\parallel,\,\omega)$ from the self-consistent solution of Eq. (7). Here, $Z^* = 1$, $T = 4\,\mathrm{K}$, $E_F = \hbar^2 k_F^2/2\mu^*$, $\epsilon_d = 13.3$, $\mathcal{L}_0/L_W = 10$, $\rho_1 = 3.0 \times 10^6\,\mathrm{cm}^{-1}$, $\rho_2 = 2.5 \times 10^6\,\mathrm{cm}^{-1}$, $\rho_0 = 1.5 \times 10^6\,\mathrm{cm}^{-1}$, $\Delta\rho = 1.0 \times 10^6\,\mathrm{cm}^{-1}$, and $\kappa = 10$. The other parameters are the same as those in Fig. 2. Results for the real part of $\Gamma_{n,n'}(q_\parallel,\,\omega)$ with $n = n' = 1$, $n = n' = 2$ and $n = 1$, $n' = 2$ are presented in (a), (b) and (c), respectively, while the result for the imaginary part of $\Gamma_{1,2}(q_\parallel,\,\omega)$ is displayed in (d). Here, both subbands are occupied.

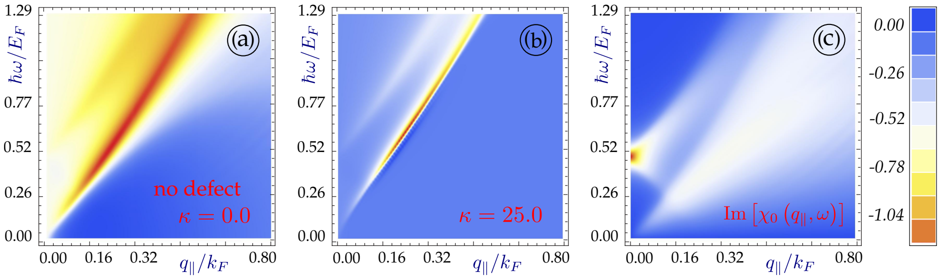

FIG. 4: Density plots for $1/\text{Re}\{\mathcal{D}et[\overleftrightarrow{\epsilon}(q_\parallel,\omega)]\}$ associated with two intealayer plasmon modes in (a) & (b), as well as for $\text{Im}\{\chi^{(0)}_{n,n}(q_\parallel,\omega)\}$ [in units of $(2\mu^*/\hbar^2)$] related to two particle-hole continua in (c) with $n = 1$, 2, where the dimensionless dielectric-function matrix $\overleftrightarrow{\epsilon}(q_\parallel,\omega)$ is defined in Eq. (4). In addition, $\kappa = 0$ in (a) & (c) while $\kappa = 25$ in (b). The other parameters used in calculations are the same as those in Figs. 2 and 3.

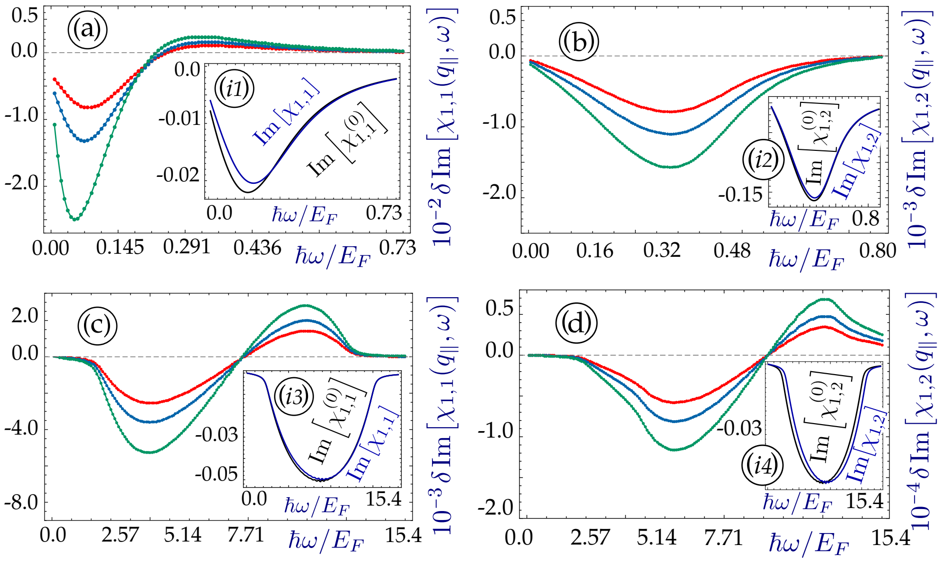

FIG. 5: $\delta\text{Im}[\chi_{1,1}(q_\parallel,\,\omega)]$ [(a), (c)] and $\delta\text{Im}[\chi_{1,2}(q_\parallel,\,\omega)]$ [(b), (d)] calculated from Eq. (1) as functions of $\hbar\omega/E_F$ for $\kappa = 5$ (red), 7 (blue), 10 (green). Here, the used parameters and units for $\chi^{(0)}_{n,n'}(q_\parallel,\,\omega)$ are the same as those in Figs. 2−4. Results are shown for $q_\parallel/k_F = 0.1$ [(a), (b)] and 2.5 [(c), (d)]. The inset of each panel compares the bare $\text{Im}[\chi^{(0)}_{n,n'}(q_\parallel,\,\omega)]$ and screened $\text{Im}[\chi_{n,n'}(q_\parallel,\,\omega)]$ under RPA in the absence of defects.

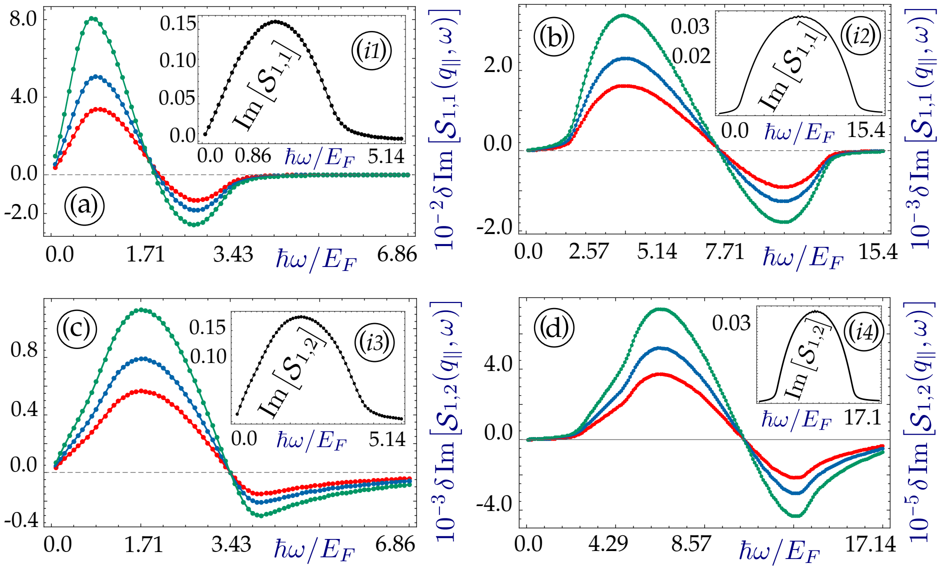

FIG. 6: Changes of loss function $\delta\mathrm{Im}[\mathcal{S}_{n,n'}(q_\parallel,\,\omega)]$ calculated from Eq. (23) as functions of $\hbar\omega/E_F$ in the single quantum well for $q_\parallel/k_F = 1.0$ [(a), (c)] and $q_\parallel/k_F = 2.5$ [(b), (d)] with $\kappa = 5$ (red), 7 (blue), 10 (green). The inset of each panel displays the dimensionless loss function $\mathrm{Im}[\mathcal{S}_{n,n'}(q_\parallel,\,\omega)]$ in the absence of defects. Here, the parameters used in numerical calculations are the same as those in Figs. 2 and 3.

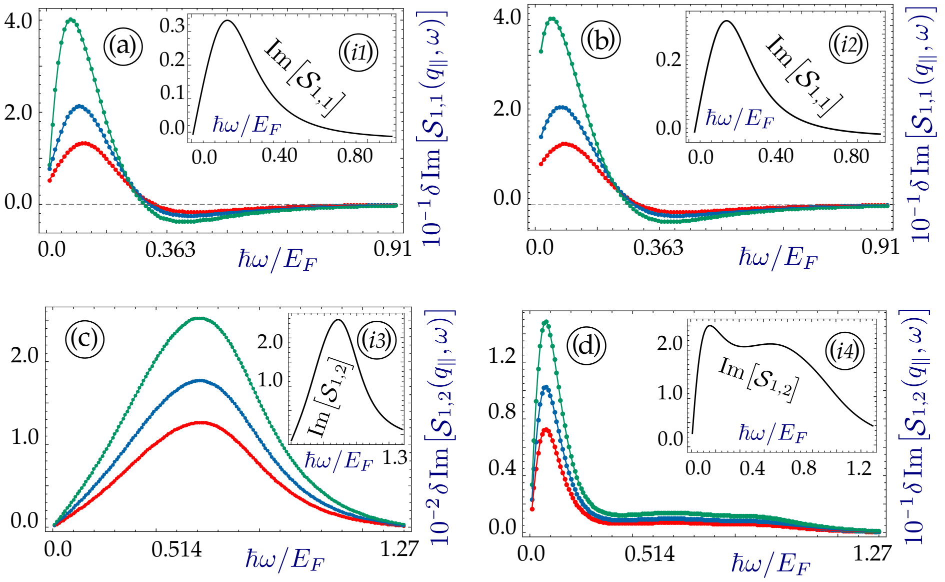

FIG. 7: Changes of loss function $\delta\mathrm{Im}[\mathcal{S}_{n,n'}(q_\parallel,\,\omega)]$ calculated from Eq. (23) as functions of $\hbar\omega/E_F$ in single and multiple quantum wells at $q_\parallel/k_F = 0.1$ for $N_L = 1$ [(a), (c)] and $N_L = 3$ [(b), (d)] with $\kappa = 5$ (red), 7 (blue), 10 (green). For defect distribution, we still use $\rho_d(z_0)/\kappa = \rho_1\Theta(-z_0 - L_W/2)] + \rho_2\Theta(z_0 - L_W/2) + [\rho_0 + z_0(\Delta\rho/L_W)]\Theta(L_W/2 - |z_0|)$ for each quantum well and two outer barriers, while $\rho_d(z_0)/\kappa$ is set to ρ_2 for the regions between two adjacent quantum wells. The inset of each panel displays $\mathrm{Im}[\mathcal{S}_{n,n'}(q_\parallel,\,\omega)]$ in the absence of defects. Here, $a/L_W = 4$ in (b), (d) and the other parameters used in numerical calculations are the same as those in Figs. 2 and 3.

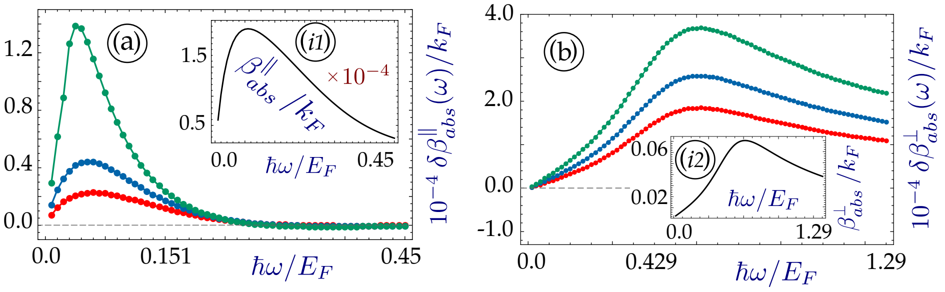

FIG. 8: Changes of intrasubband $\delta\beta^{\parallel}_{abs}(\omega)$ and intersubband $\delta\beta^{\perp}_{abs}(\omega)$ absorption coefficients (in units of k_F) calculated from Eqs. (35) and (38) as functions of $\hbar\omega/E_F$ for $N_L = 1$ and $\kappa = 5$ (red), 7 (blue), 10 (green). The insets $(i1)$ and $(i2)$ present $\beta^{\parallel}_{abs}(\omega)$ and $\beta^{\perp}_{abs}(\omega)$ (in units of k_F) in the absence of defects. Here, $k_F\mathcal{R}_0 = 50$ and the other parameters used in numerical calculations are the same as those in Figs. 2 and 3.

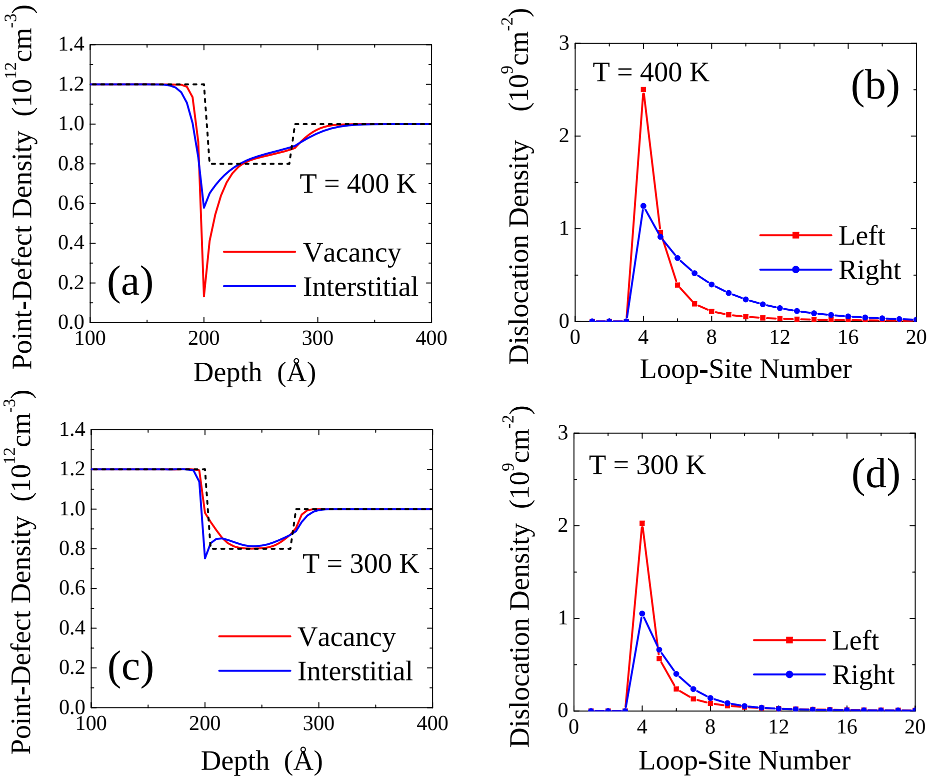

FIG. 9: Concentrations of point vacancies $c_v^j(z)$ and interstitials $c_i^j(z)$ $[(a),\,(c)]$, and dislocation-loop densities $\sigma_{dl}^j(\ell)$ at two interfaces $[(b),(d)]$, in an AlAs-205Å/InAs-75Å/GaAs-255Å single quantum well at $T=400\,$K $[(a),(b)]$ and 300 K $[(c),(d)]$. Here, $\mathcal{G}_0^j$ are 4.6, 0.9, 2.1 in units of $10^{17}\,\text{cm}^{-3}\,\text{sec}^{-1}$ and c_{FP}^j are 1.2, 0.8, 1.0 in units of $10^9\,\text{cm}^{-3}$ for $j=1,\,2,\,3$. In addition, σ_0^j are 2.0, 1.0 in units of $10^9\,\text{cm}^{-2}$ for $j=1,\,2$. The values for other parameters, i.e., bias factors, absorption and emission rates, diffusion coefficients, have been obtained from crystal symmetries [1] and by scaling melting temperatures with respect to SiC materials [47].

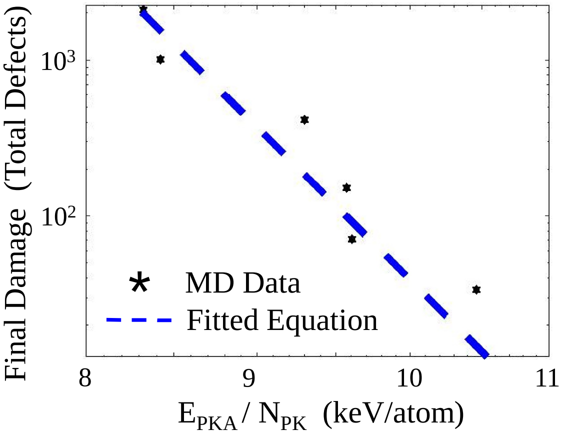

FIG. 10: Total number $\mathcal{N}_{MD}(\varepsilon_T)$ of defects in MD simulation as a function of the PKA energy $E_{PKA} \equiv \varepsilon_T$ scaled by the number N_{pk} of defects at the peak time in Fig. 11, where the formula $\mathcal{N}_{MD}(\varepsilon_T) = \mathcal{A}_0[\varepsilon_T(\text{keV})]^n$ and $N_{pk} = B_0[\varepsilon_T(\text{keV})]^\ell$ with parameters $\mathcal{A}_0 = 75.07$, $n = 1.11$, $B_0 = 64.15$, and $\ell = 1.04$ extracted from fitting (dashed curve). Here, the display is in logarithm scale with a straight-line dependence, while the fitting is done in linear scale with an exponential dependence. Here, the fitting result is presented on a logarithm scale with a straight-line-like dependence, while the fitting is done for a linear scale with an exponential dependence which requires a delicate fitting process.

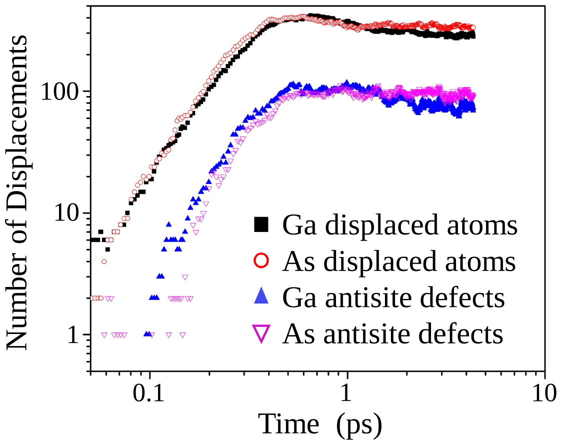

FIG. 11: The number of Ga and As displaced atoms and antisite defects as a function of time in a $\varepsilon_T = 10\,\text{keV}$ Ga-PKA cascade in GaAs, where the peak time about 0.8 ps is found.

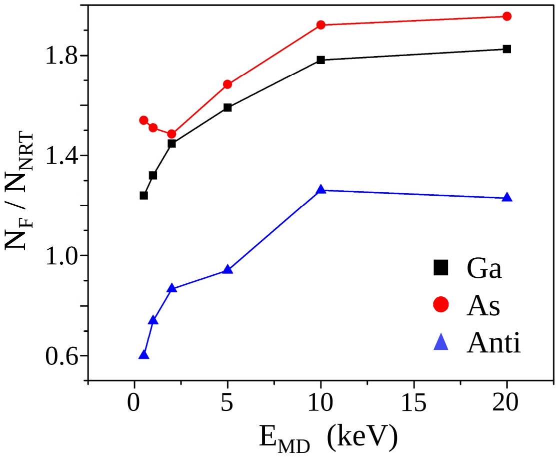

FIG. 12: The number $\mathcal{N}_F(\varepsilon_T)$ of Ga and As displaced atoms and antisite defects as a function of recoil energy $E_{MD} \equiv \varepsilon_T$ in MD simulation at $t = 10\,\mathrm{ps}$, where the NRT result is given by $\mathcal{N}_F(\varepsilon_T) = 0.8\,\varepsilon_T/2E_d$.

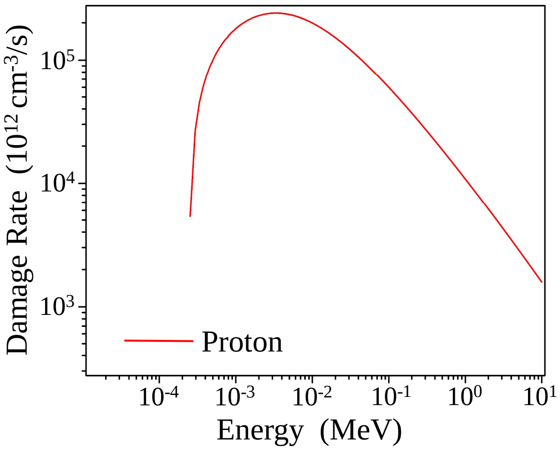

FIG. 13: Calculated defect production (or damage) rate $\mathcal{G}_0(E_i)$ per unit volume as a function of the incident-proton kinetic energy E_i. Here, the proton flux is assumed to be a constant $3.0 \times 10^{12}\,\mathrm{cm}^{-2}\cdot\mathrm{sec}^{-1}$.